STRUCTURAL AND FUNCTIONAL ANALYSIS OF CORTICAL 3-HINGE GYRAL JOINTS

by

FANGFEI GE

(Under the Direction of Tianming Liu)

ABSTRACT

Understanding the complex folding patterns on cerebral cortex has been of great interest and importance. As a typical brain anatomical pattern on gyri, 3-hinge gyral joint introduces a novel way to analyze cortical folding patterns in terms of gyral hinge numbers. In fact, 3-hinges are of unique structural and functional importance in terms of structural and functional features, brain development and brain evolution and has the potential to determine inter-subject or even inter-species correspondence. A variety of recent studies have demonstrated the distinct anatomical characteristics of 3-hinge gyral joints compared to other gyral regions, like its thicker cortices and it has more diverse connected fibers’ end orientations. However, the mechanism of 3-hinge gyri formation and its potentially different functional role have been rarely explored so far. To bridge this gap, I did some relevant studies from both structural and functional perspective to better understand the formation mechanism and the potential functional characteristic of 3-hinge gyri.

INDEX WORDS: 3-hinge, structural analysis, functional analysis, cortical folding, fiber density, convolutional neural network, neural architecture search

STRUCTURAL AND FUNCTIONAL ANALYSIS OF CORTICAL 3-HINGE GYRAL JOINTS

by

FANGFEI GE

BS, Northwestern Polytechnical University, China, 2013

A Dissertation Submitted to the Graduate Faculty of The University of Georgia in Partial Fulfillment of the Requirements for the Degree

DOCTOR OF PHILOSOPHY

ATHENS, GEORGIA

2019

STRUCTURAL AND FUNCTIONAL ANALYSIS OF CORTICAL 3-HINGE GYRAL JOINTS

by

FANGFEI GE

Major Professor:	Tianming Liu
Committee:	Jaewoo Lee
	Xianqiao Wang

Electronic Version Approved:

Suzanne Barbour
Dean of the Graduate School
The University of Georgia
August 2019

DEDICATION

This dissertation is dedicated to my loving parents Ming Ge and Hui Zhao, for their continuous support and tremendous encouragement during my Ph.D. study, especially during the darkest time approaching graduation.

ACKNOWLEDGEMENTS

First of all, I would like to express my sincerest appreciation to my major professor, Prof. Tianming Liu. Without the valuable opportunity he offered to me, plus his patient guidance and persistent support, this dissertation, along with all the related publications would not have been possible. His attitude in doing researches as well as his vision in the development of brain imaging analysis keep impressing me and have been guiding me during my research career even when I was in China. It has always been a great time being part of the team in Dr. Liu's research lab.

Second, I would like to thank my committee members, Dr. Xianqiao Wang and Dr. Jaewoo Lee, for their insightful feedback and interactions. Each time after my comprehensive exam and my prospectus presentation, they provided me with helpful suggestions in improving my dissertation work as well as in how to do well in a job interview, which benefits me a lot.

In addition, I would also like to thank my colleagues and collaborators, especially those senior to me, who has ever offered me tremendous help when I was junior in the lab. It's a pleasure to work with them and solve problems together. Without their help in both research and life, I would not have gone so far.

Finally, I would like to thank my loving family, for their support, encourage and sacrifices. Their trust and help is precious through 6 years of my Ph.D. life, both in China and US.

TABLE OF CONTENTS

Page

CHAPTER

LIST OF TABLES

LIST OF FIGURES

Page

CHAPTER 1

INTRODUCTION

1. What Is 3-hinge Gyral Joint

As we know, one of the most prominent features of human brain lies in the high-level convolution of cerebral cortex. During brain development, the cerebral cortex undergoes substantial folding, leading to intricate arrangements of convex gyri and concave sulci [1-4]. Modern magnetic resonance imaging (MRI) techniques enable in vivo studies of the cortical folding patterns, which attract growing research interest. As an essential characteristic of the human cerebral cortex, the fold has shown quite different patterns on even major gyri and sulci across subjects [5-8]. In spite of this great variability, the folding pattern of human cortex seems to be closely related to the architectonic, connectional and functional specialization of the cortical surface [8]. Evidence has also shown that the folding pattern of human cerebral cortex can benefit cytoarchitectonic areal parcellation [9], normal maturation and neurodegenerative process investigation [10] and abnormal brain development understanding [11].

Emerging studies have reported that gyri and sulci exhibit distinct patterns from the perspectives of anatomy [12, 13], morphology[14], structural connectivity [15, 16] and function [17-20]. For example, microcosmic studies at the cellular level revealed that the subventricular zone (a secondary proliferative zone containing neural progenitor cells) during embryonic life is thicker in areas underlying gyrus formation and thinner in areas underlying sulcus formation [12, 13]. A similar finding in the neocortex of both developing infants and healthy adults is that cortical thickness is significantly thicker at the crown of gyri and normally thinner in the depth of sulci [12, 17, 21]. Meanwhile, under the mechanical impact of cortical folding, dendritic shapes in deep gyral and sulcal layers are different [17]. What’s more, gyri and sulci have different morphologic traits during aging process. Gyri become more sharply and steeply curved while the sulci become more flattened and less curved [14]. More recently, investigations into the neuronal pathways demonstrated that axonal streamline fibers in the human brains tend to course horizontally around the sulcal surface but orient tangentially to the gyral surface [22-25]. Similar observations suggest that the fiber terminations dominantly concentrate on gyri rather than sulci, which is evolutionarily preserved in the cortical architectures of primate brains [24, 26]. Joint representation of multimodal neuroimaging data, including diffusion tensor imaging and fMRI found that both structural and functional connectivity patterns are strong among gyri, weak among sulci, and moderate between gyri and sulci [15].

Taken together, all the above-mentioned studies across multiple disciplines have consistently brought insights into fundamental differences between gyri and sulci. However, on gyri, there still exists a sub-population with particular convolution pattern described by the number of hinges, called 3-hinge gyral folding pattern, which was first introduced in our previous studies [8]. Motivated by the mounting findings of gyri and sulci differences, in this dissertation, it mainly focuses on the exploration of 3-hinge (one of the sub-populations of gyri) and investigates its characteristics in both structural and functional aspects. Specifically, a 3-hinge gyral joint is a conjunction of gyri coming from multiple directions, which is also where three gyral crests meet. Exemplar 3-hinge gyral joints are represented by colored bubbles as shown in Figure 1.1.

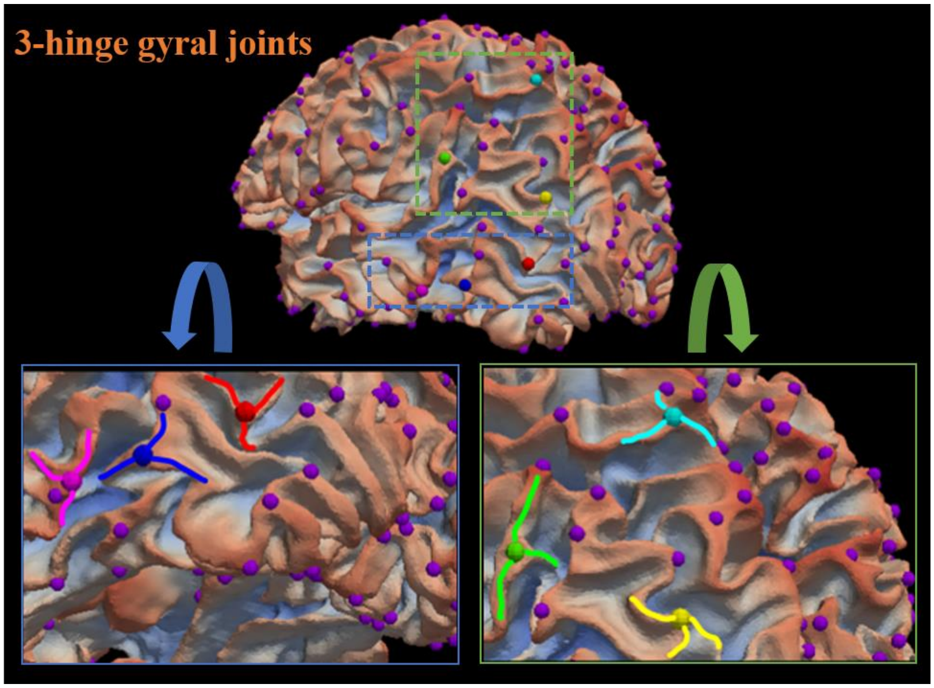

Figure 1.1. Exemplar 3-hinge gyral joints (colored bubbles) visualization. Here, six randomly selected 3-hinge gyral joints are zoomed in and their corresponding gyral crests can also be visualized.

2. Why is 3-hinge Gyral Joint Important in Brain Analysis

In fact, 3-hinge gyral joints ("3-hinge" for short sometimes) are of unique structural and functional importance in terms of structural and functional features, brain development and brain evolution which also have the potential to determine inter-subject correspondence. In our previous works, it has been demonstrated that 3-hinges have thicker cortices [27] and diversities [28, 29], and are more strongly functionally connected compared to other gyral regions [18-20, 30]. In terms of brain development, we found in our previous works that the 3-hinges with complicated morphology tend to have more diverse connected fibers' end orientations [29]. In other words, the orientation of fiber terminations closely follows the curvedness of 3-hinge gyral crest. These conclusions are in line with our previous works and add new knowledge to our previous DTI-based findings that axonal fiber terminations concentrate on gyri. All these findings suggest a close relationship between gyrification and axonogensis. In addition, we also found some consistent fiber connectivity patterns from the corresponding 3-hinges across individuals and species [31]. Recently, a quantitative examination of gyral folding patterns across primate species showed that the complexity of 3-hinge gyral folding patterns successively expressed from macaque brain to human brain, in which 6 popular and cross-species consistent 3-hinge gyral folds in macaque/chimpanzee/ human brains were quantitatively identified and characterized, 2 unique 3-hinges in macaque brains, 6 unique ones in chimpanzee brains and 14 unique ones in human brains [28]. These above-mentioned findings suggest that 3-hinge convolutions could be an emergent phenomenon necessitated by some underlying function or structure which show the promise of analyzing 3-hinge from both structural and functional perspectives.

As a convoluted surface, the neocortex is usually represented by a reconstructed mesh surface, upon which quantitative analyses are performed [32]. The folding pattern of human cerebral cortex is a multi-scale concept whose research scope can vary from a very small neighborhood to a whole brain cortical surface [8]. The widely used folding pattern descriptors in the literature can be classified into two groups – global and local descriptors [8]. Global measurements such as surface area [33], gyrification index [34], and spherical wavelets [35] quantify the cortical convolution level of the whole brain or preselected regions of interest (ROIs). In contrast, local descriptors, such as surface curvature, estimate the cortical folding pattern vertex-wise in a small area. Some recent works also extend the global descriptors, such as gyrification index to local scales [36, 37]. However, 3-hinge can serve as a novel way that combines both advantages of parametric method (achieving compact representation of morphology pattern) and surface profiling method (achieving flexibility of arbitrary morphology representation) to analyze cortical folding patterns in terms of gyral hinge numbers, which is also a good meso-scale anatomical landmark since it is relatively easier to identify without ambiguity. Therefore, from the methodological perspective, analyzing 3-hinge is of great importance considering its methodological advantage and the deep insights it can provide into the mechanism of brain development and evolution.

3. How to Identify 3-hinge Gyral Joint

There are mainly two automatic approaches for identifying 3-hinge gyral joints, both of which are used in this dissertation.

The first approach is based on that proposed in Li's work [8] which includes two rounds of surface profiling. In the first round, all vertices on the surface need to be classified into two groups, gyri and sulci. A 3D coordinate system is built for every vertex on the cortical surface, as there exists a normal direction as the Z direction, as well as a tangent plane represented by a 2D polar coordinate system. The initial direction in the polar coordinate system is randomly selected. Then each vertex's surface patch is sampled into 72 evenly distributed spokes from the initial direction. After that a power function is applied to fit the model of each spoke. The parameters of the model are evaluated in a least-square sense with Levenberg–Marquardt algorithm and the values of these parameters could be used to extract features of any vertex on the surface. These features include average ratio, average concave, average convex and sulci or gyri. With these extracted features, it can classify each vertex into two categories: gyri or sulci. In the second round, an inflated surface is generated by FreeSurfer. The second profile of each point is then generated on the inflated surface. For each cortical vertex, the profile process is the same as the first profile on the original surface with 72 evenly distributed spokes. Each point is projected onto the inflated surface and could be classified to gyri or sulci group. The goal is to identify 3-hinge vertex on gyri; therefore, only the profiles of vertices on gyri are considered. Then the spokes are classified into two types — either all points are on gyri or only part of them are on gyri. For the profile of a vertex, the adjacent all-gyri spokes are clustered into a group and the vertex involving three all-gyri spoke groups is taken as 3-hinge vertex. Finally, it clusters the adjacent 3-hinge vertices and each cluster is taken as 3-hinges. The vertex closest to the center of the cluster is taken as the center vertex of 3-hinges. More details and pipeline can be found in Chapter 2, Section 3.3.

The second approach was proposed by Chen’s work recently which developed automatic data processing and analysis pipeline that is capable of handling big datasets to extract 3-hinges based on a ‘gyral net’ system [32]. Generally, the pipeline includes two major steps as illustrated in Figure 1.2: (a) gyral crest segmentation (Figure 1.2 (d)-(e)) and (b) gyral crest skeleton extraction (Figure 1.2 (f)). For gyral crest segmentation step, it is to segment gyral crest from cortical surfaces. For each surface vertex, it computes its gyral altitude defined as the movement in the surface normal direction from its original location to the “mid-surface,” a smoothed and inflated mid-line that separates gyri from sulci. Vertices above the “mid-surface” have positive altitude values and otherwise they are assigned negative values (Figure 1.2 (d)). Based on gyral altitude, the watershed algorithm is adopted to progressively segment the gyral crest (regions over an altitude level) from sulcal basins. For gyral crest skeleton extraction step, it is to extract gyral crest lines. Based on these lines, the junctions where multiple lines meet were identified as the centers of 3-hinges. Generally, gyral skeletons are the crest curves located in the central parts of gyri, which are the furthest locations on gyral regions from the borders between gyral crests and sulcal basins. Here, the method detailed in [32] is an enhanced version of the one in [8]. First, distance transform is conducted on the segmented gyral area to highlight the center of gyral crest. Then, the first tree marching starts from the local centers of gyral crest and successively connected the vertices to form multiple tree-shape graphs. After connecting the trees, the redundant branches were pruned and only the major branches were left and taken as the skeleton of gyral crest (black curves in Figure 1.2 (b)). The skeleton forms a gyral network, vertices on this network with degrees equal to 3 are 3-hinge vertices defined as gyral joints.

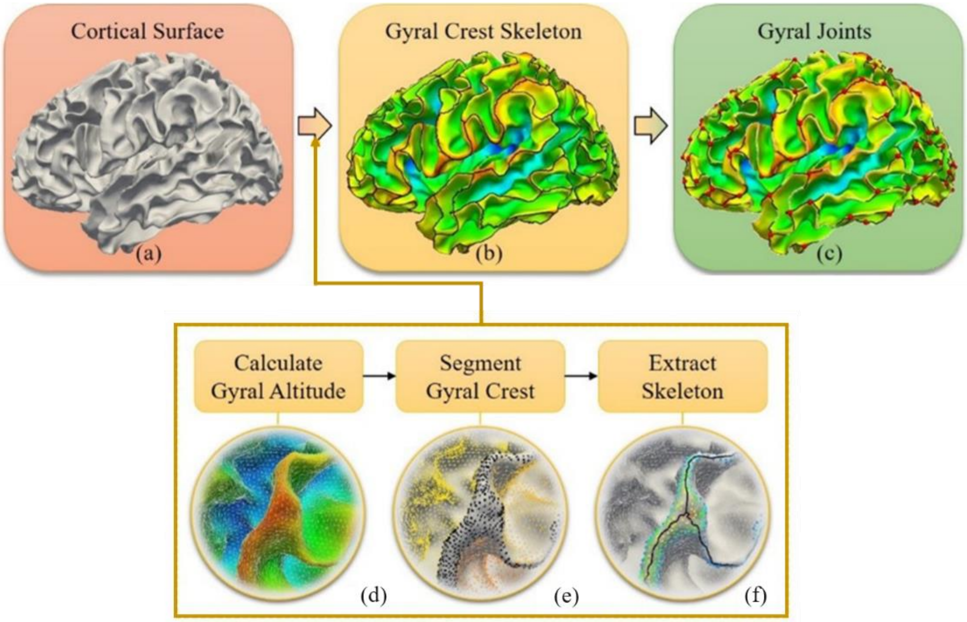

Figure 1.2. Pipelines of the extraction of gyral skeleton and 3-hinge. (a) Cortical surface of the white matter/gray matter boundaries. (b) Black curves are the extracted skeleton of gyral crest. The cortical surface is color-coded by gyral altitude. Red regions have high gyral altitude values while blue regions have low values. (d-f) Steps of extracting gyral crest skeleton. Gyral altitude is computed first in (d), based on which cortical surface is segmented into gyral crest (black dots in (e)) and sulci. Finally, the gyral crest is skeletonized.

4. Contributions

This dissertation does analyses on both structural and functional characteristics of 3-hinge gyri. Consequently, its contributions are two folds, in structural and functional aspect respectively.

For the structural analysis of 3-hinge gyri, although previous study has already analyzed the regularity and variability of cortical folds across human, chimpanzee and macaque brains based on 3-hinge gyral fold descriptor, the possible mechanisms of formation of such cross species preserved 3-hinge gyri in primate brains has not been explored yet. To bridge this gap, in my experiment, I firstly extracted 3-hinge gyral regions in macaque/chimpanzee/human brains, then quantified and compared the relevant DTI-derived fiber densities in 3-hinge and 2-hinge gyral regions. According to the initial comparison results which consistently show that DTI-derived fiber densities in 3-hinge regions are much higher than those in 2-hinge regions, a hypothesis that besides the cortical expansion, denser fiber connections can induce the formation of 3-hinge gyri was proposed. This hypothesis was also further consolidated by designed computational simulation models later. To summarize, this work (Chapter 2) proposes a plausible theory of 3-hinge gyri formation and also provides new insights into structural and functional cortical architectures and their relationship.

For the functional analysis of 3-hinge gyri, considering the strong correlation between brain structure and function and motivated by some preliminary findings on the different functional roles of gyri and sulci [18-20, 30, 38, 39], 2-hinge and 3-hinge as two potential sub-populations on gyri, possible functional differences between them are investigated from the perspective of neural activity in Chapter 3 and Chapter 4. Here, the work in Chapter 3 mainly focuses on the exploration of the different functional roles of neural activities under resting state in gyral, sulcal, 2-hinge and 3-hinge areas, while the work in Chapter 4 is an extension which pays more attention to the improvement of the classification model architecture, the methodological contribution of which is the AdaNet-based NAS framework.

5. Dissertation Outline

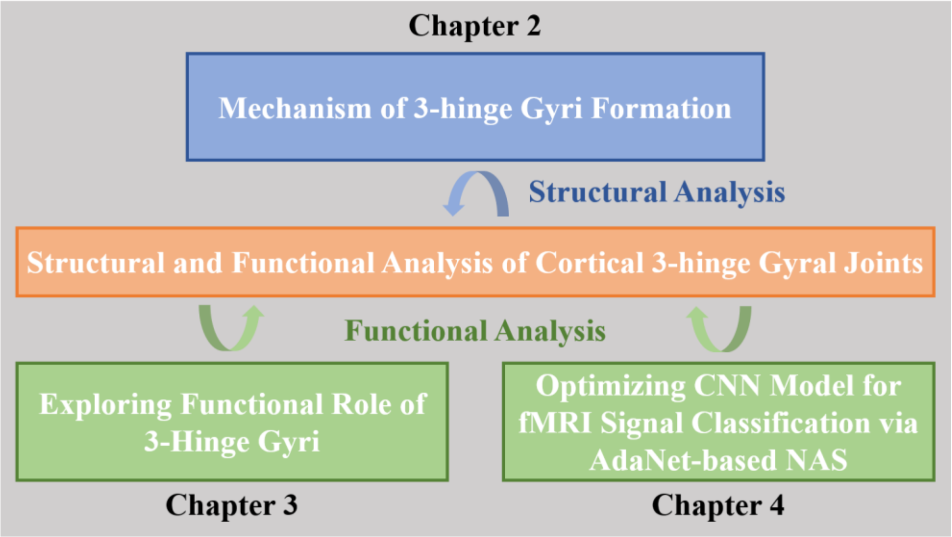

Figure 1.3. Dissertation overview.

As illustrated in Figure 1.3, this dissertation mainly contains three parts corresponding to Chapters 2-4, respectively. Chapters 2 explores the mechanism of 3-hinge gyri formation from structural perspective which does a structural analysis of cortical 3-hinge gyral joint. Chapters 3-4 investigates the different functional role of 3-hinge gyri from functional perspective, corresponding to the functional analysis. Chapter 5 is the conclusions and future work.

CHAPTER 2

DENSER GROWING FIBER CONNECTIONS INDUCE 3-HINGE GYRAL FOLDING[1]

---

[1] Fangfei Ge, Xiao Li, Mir Jalil Razavi, Hanbo Chen, Tuo Zhang, Shu Zhang, Lei Guo, Xiaoping Hu, Xianqiao Wang and Tianming Liu. "Denser Growing Fiber Connections Induce 3-hinge Gyral Folding." *Cerebral Cortex* 28, no. 3 (2017): 1064-1075.
Reprinted here with permission of the publisher.

1. Abstract

In this chapter, I do an advanced analysis on 3-hinge gyral joints from the structural perspective which explores the relationship between the axonal fiber connection and 3-hinge gyral folding.

Recent studies have shown that quantitative description of gyral shape patterns offers a novel window to examine the relationship between brain structure and function. Along this research line, this chapter examines a unique and interesting type of cortical gyral region where three different gyral crests meet, termed 3-hinge gyral region. We extracted 3-hinge gyral regions in macaque/chimpanzee/human brains, quantified and compared the relevant DTI-derived fiber densities in 3-hinge and 2-hinge gyral regions. Our observations consistently show that DTI-derived fiber densities in 3-hinge regions are much higher than those in 2-hinge regions. Therefore, we hypothesize that beside the cortical expansion, denser fiber connections can induce the formation of 3-hinge gyri. In order to examine the biomechanical basis of this hypothesis, we constructed a series of three-dimensional finite element soft tissue models based on continuum growth theory to investigate fundamental biomechanical mechanisms of consistent 3-hinge gyri formation. Our computational simulation results consistently show that during gyrification gyral regions with higher concentrations of growing axonal fibers tend to form 3-hinge gyri. Our integrative approach that combines neuroimaging data analysis and computational modeling appears effective in probing a plausible theory of 3-hinge gyri formation and providing new insights into structural and functional cortical architectures as well as their relationship.

2. Background and Motivation

Convoluted cortical folding is a prominent feature of the primate brains [24, 40]. Convolution may arise at multiple stages, primary, secondary and tertiary which occurs over a period of several months [41, 42]. Primary folding is notably preserved among individuals [43] while secondary and tertiary foldings vary cross individuals and evolve after primary folding is completed [44], which it is believed that differential growth of the cortex is a possible stimulus for secondary and tertiary folding [45, 46]. Neuroscientific studies have demonstrated that neural structures of concave sulci and convex gyri emerge from a complex cortical folding process in brain development [3]. It has been shown that cortical fold patterns seem to be closely correlated with neurodevelopment [27, 47-49], cytoarchitecture [50, 51], and cognitive functioning [52-55]. Therefore, a quantitative description of complex cortical folding patterns is of fundamental importance to understand the underlying structural [6, 56-58] and functional [15, 59-61] mechanisms of the brain. Essentially, the folding pattern of human cerebral cortex is a multi-scale concept, and therefore the research scope of quantitative description of cortical folding can vary from a very small neighborhood on the cortex to the entire cortical surface [8]. In previous studies, descriptors proposed for modeling and analyzing cortical folding patterns can be classified into two major categories [8]. The first one was based on the descriptor of curvature and its derivations [62-64]. The other one was a global descriptor, the studies of which usually use tools like gyrification index [34, 65], spherical wavelets [35, 66] and intrinsic curvature [67] to quantity the convolution level of the whole cortical surface or a preselected regions of interests (ROIs). In general, both categories of cortical folding descriptors unveiled interesting properties of cerebral cortex and helped understand the regularity and variability of the complex cerebral cortex.

Recently, inspired by the work on folding pattern analysis of rocks in geology, Li et al proposed a novel way that combined both advantages of parametric method and surface profiling method to analyze cortical folding patterns in terms of gyral hinge numbers [8]. Basically, as illustrated in Figure 2.1, gyral crests with white curves in Figure 2.1 are termed 2-hinge gyri while regions where three 2-hinge gyral crests meet are termed 3-hinge gyri as highlighted by the yellow spheres in Figure 2.1. It is worth to note [8] that four gyral crests rarely meet to form 4-hinge gyri. Thus, in this chapter, we will mainly focus on the discussion of 2-hinge and 3-hinge gyri. Notably, in our recent study [40], we quantitatively identified and characterized six popular and cross-species consistent 3-hinge gyral folds in macaque/chimpanzee/human brains, two unique 3-hinges in macaque brains, six unique ones in chimpanzee brains and fourteen unique ones in human brains. Our quantitative measurements applied to these 3-hinge gyral folds showed the increasing complexity among the primate species we analyzed. However, this prior study [40] did not explore the possible mechanisms of formation of such cross-species preserved 3-hinge gyri in primate brains which is the main objective of this study.

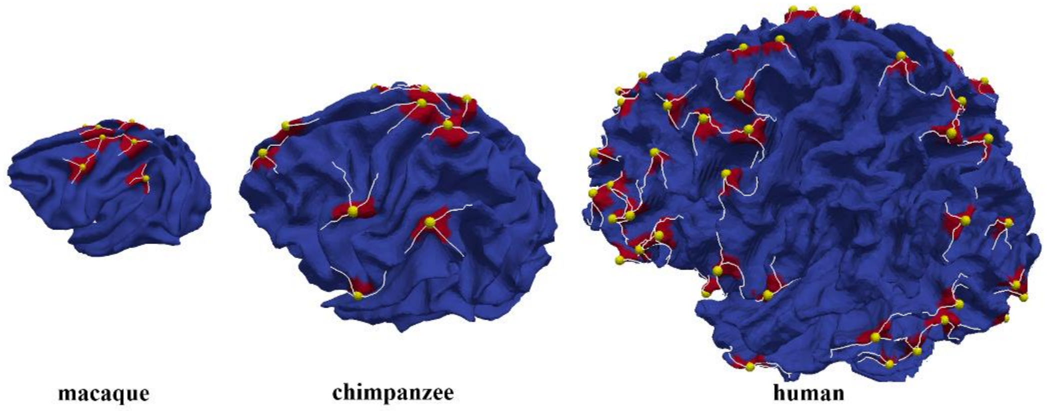

Figure 2.1. Illustration of 2-hinge and 3-hinge gyral folds in macaque, chimpanzee and human brains.

Specifically, we first extracted the 3-hinge gyral regions in macaque /chimpanzee/human brains by using the automated computational pipeline in [8] Then, based on the 3-hinge gyri on the whole cortical surface, we quantified the densities of diffusion tensor imaging (DTI) -derived fibers connected to these 3-hinge gyral regions, as well as those connected to 2-hinge gyri. Finally, we quantitatively compared the DTI-derived fiber densities in 3-hinge and 2-hinge gyral regions in the entire macaque/chimpanzee/human brains. Our results consistently demonstrate that DTI-derived fiber densities in 3-hinge gyri are much higher than those in 2-hinge gyri. Therefore, we hypothesize that beside the cortical expansion, denser fiber connections can induce the formation of 3-hinge gyri. By constructing a series of three-dimensional finite element soft tissue models based on continuum growth theory, we investigated fundamental biomechanical mechanisms of consistent 3-hinge gyri formation and examined the biomechanical basis of this hypothesis.

3. Methods

3.1 Overview of computational framework

Basically, there are 4 major computational steps in this work. 1) We modified and employed an automatic computational pipeline to identify 2-hinge and 3-hinge gyral folding patterns across entire primate brain. 2) We quantified the DTI-derived fiber density [25] termed as the number of fibers per unit surface area, over the entire cerebral cortex. 3) We derived the DTI-derived fiber densities on the extracted 2-hinge and 3-

hinge gyral regions, and then performed extensive comparisons between them. 4) We designed and constructed a series of computational finite element models to investigate the fundamental mechanism of 3-hinge formation. In general, our integrative approach which combines neuroimaging data analysis over macaque/chimpanzee/human brains and computational simulations provides a unique window to understand the deeply rooted regularity of 3-hinge gyri formation and offers a plausible theory that denser growing fiber connections induce 3-hinge gyri formation.

3.2 Data description and preprocessing

Imaging data of human brains. In this work, DTI images were used to perform the reconstruction of cortical surfaces. In total, 64 human brains from the Q1 release of WU-Minn Human Connectome Project (HCP) consortium [68] were used in this study, and the age range of these subjects is 22-35 years. For T1-weighted structural MRI, the scan protocol used a TR=2400ms, TE=2.14ms, flip angle=8deg, image matrix=260×311×260 and resolution=0.7×0.7×0.7mm^3. DTI data collected with spin-echo EPI sequence was acquired using the following parameters: TR=5520ms, TE=89.5ms, flip angle=78deg, FOV=210×180, matrix=168×144, resolution=1.25×1.25×1.25mm^3, and echo spacing=0.78ms. Particularly, a full DTI session includes 6 runs, representing 3 different gradient tables, with each table acquired once with right-to-left and left-to-right phase encoding polarities, respectively. Each gradient table includes approximately 90 diffusion weighting directions plus 6 b=0 acquisitions interspersed throughout each run. Diffusion weighted data consisted of 3 shells of b=1000, 2000, and 3000s/mm^2 interspersed with an approximately equal number of acquisitions on each shell within each run. White matter cortical surface reconstructed using DTI data was based on FA maps via the methods in [69] after performing skull removal, motion correction, eddy current correction and tissue segmentation based on FSL [70].

Imaging data of chimpanzees. All the 16 chimpanzee subjects (all females, 29.4±12.8 years) used here were members of a colony in the Yerkes National Primate Research Center (YNPRC) at Emory University in Atlanta, Georgia. All imaging studies were approved by the IACUC of Emory University. Prior to scanning, the subjects were immobilized with ketamine injections (2−6 mg/kg, i.m.) and were subsequently anesthetized with an intravenous propofol drip (10 mg/kg/hr) according to standard veterinary procedures used at YNPRC. The subjects remained sedated for the duration of the scans as well as the time needed for transportation between their home cage and the scanner location. After completing scans, chimpanzees were temporarily housed in a single cage for 6 to 12 hours to allow effects of anesthesia to wear off before being returned to their home cage and cage mates. The veterinary staff and research staff assessed the general well-being (i.e., activity, food intake) of the chimpanzees twice daily after the scan for possible distress associated with aesthetic accesses.

The anatomical MRI scans were performed on a Siemens 3T Trio scanner with a standard birdcage coil. Foam cushions and elastic straps were used to minimize head motion. T1-weighted MRI images were acquired with a 3D magnetization-prepared rapid gradient echo (MPRAGE) sequence for all participants. For subjects scanned using the MS-EPI (multi-shot double spin-echo echo planar imaging) sequence, the scan protocol, optimized at 3T used a TR=2400ms, TE=4.13ms, flip angle=8 deg, image matrix=256×256×192 and resolution=$1.0\times1.0\times0.8\,\mathrm{mm}^3$, with 2 averages. For subjects scanned using SS-EPI (single-shot double spin-echo echo planar imaging), the scan protocol is similar, despite that the resolution $=0.8\times0.8\times0.8mm^3$ isotropic. In this study, MRI images from 16 female chimpanzees are used. . The preprocessing steps were similar to those used in human data processing and the brains of chimpanzees are scaled to the same size as human brain.

Imaging data of macaques. All the 20 macaque subjects (all females, 14±6.7 years) were members of a colony at YNPRC. All MRI scans were approved by IACUC of Emory University. Prior to scanning, the subjects were immobilized with ketamine injections (2−6 mg/kg, i.m.) and were subsequently anesthetized with an intravenous propofol drip (10 mg/kg/hr) following standard veterinary procedures used at YNPRC. The macaques remained sedated for the duration of the scans as well as the time needed for transportation between their home cage and the scanner location. After completing scans, macaques were temporarily housed in a single cage for 6 to 12 hours to allow the effects of anesthesia to wear off before being returned to their home cage and cage mates. The veterinary staff and research staff observed the general well-being (i.e., activity, food intake) of the macaques twice daily after the scan for possible distress associated with anaesthetic accesses.

The anatomical MRI scans were performed on a Siemens 3T Trio scanner with a standard knee oil. To minimize head motion, foam cushions and elastic straps were used during the scan. Particularly, a specially designed holding device was used to stabilize macaque’s head during scanning with 2 plastic screws anchoring in the macaque’s ear canals tightly. The high resolution T1-weighted MRI images were acquired with a 3D MPRAGE sequence. The scan protocol used a TR=2500ms, TE=3.49ms, flip angle=8 deg, image matrix=256×256×192 and resolution=0.5×0.5×0.5mm^3, with 3 averages. In this study, MRI images from 20 subjects were used. The preprocessing steps were similar to those used in human data processing and the brains of macaques are scaled to the same size as human brain.

3.3 Automatic pipeline for 2-hinge and 3-hinge gyri extraction

A gyral hinge refers to the region on the top of gyrus with the maximal folding curvature. By following and extending our prior work [8], we automatically extracted the centers of 3-hinge gyri from these reconstructed cortical surfaces in Section 3.2 [8]. A gyral hinge curve can be traced when hinges are connected along a gyral crest and the number of hinge curves intersecting together at a cross-point can be used to characterize the gyral folding patterns [8]. In order to automatically identify 3-hinge vertices, two main steps of surface profiling were proposed and used. Here we take a human brain cortical surface as an example to detail the two-step process: 1) classifying vertices into two groups, gyri and sulci in Figure 2.2(a)-(d) and 2) finding 3-hinge centers in Figure 2.2(e)-(i). Firstly, we built a local 3D coordinate system for each vertex on the cortical surface. The normal direction of the vertex was considered as the Z direction and a tangent plane was represented by a 2D polar coordinate system. Then seventy-two 20mm long spokes were allocated from the vertex along the neighboring surface patch. In total, 20 points were evenly sampled along each spoke. The projections of all spokes on the tangent plane were evenly distributed (5 degrees interval). Then a power function was expressed as follows to fit the model of each spoke:

$$y = b + y_0 \left(\frac{x}{x_0}\right)^n \tag{2.1}$$

where (x, y) is the 2D Cartesian coordinate of a profile based on the 2D polar coordinate system, x_0, y_0, b, n are parameters of the profile via a least-square fitting method. Then, features of a vertex such as average ratio, average concave, average convex, and sulci-or-gyri can be extracted via mathematical operations [8]. Particularly, the feature, sulci-or-gyri, was used to classify a vertex to be a sulcal vertex or a gyral vertex.

The second profiling step was only applied on gyral vertices on an inflated surface in order to identify centers of 3-hinge gyri. The inflated surface by FreeSurfer [71] here still retains the original topology information such as the number of vertices and the correspondence between an inflated surface (Figure 2.2(g)) and an original surface (Figure 2.2(b)). With this set-up, then 72 evenly distributed spokes and 20 evenly sampling points on each spoke were constructed. It is evident that each sampling point with a label indicates whether it is a gyrus or sulcus. Following the construction, we classify each spoke into two types – either all sampling points in this spoke are on a gyrus or only part of these points are on a gyrus. For the profile of a vertex, its adjacent all-gyri spokes were clustered into one group divided by any part-gyri spoke. If this vertex belongs to three all-gyri spoke groups, it is considered as a 3-hinge vertex. Finally, we clustered all adjacent 3-hinge vertices using spatial information and termed the vertex closest to cluster center as a 3-hinge center. In order to compute axonal fiber density of 2-hinge and 3-hinge gyral folds later, we need to define an area for each 3-hinge vertex. Here we consider the surrounding area within a radius r=6mm of a 3-hinge center as its corresponding 3-hinge area (Figure 2.2(i)). Once the area of 3-hinge vertex is determined, the 2-hinge vertex area can be found by excluding 3-hinge areas.

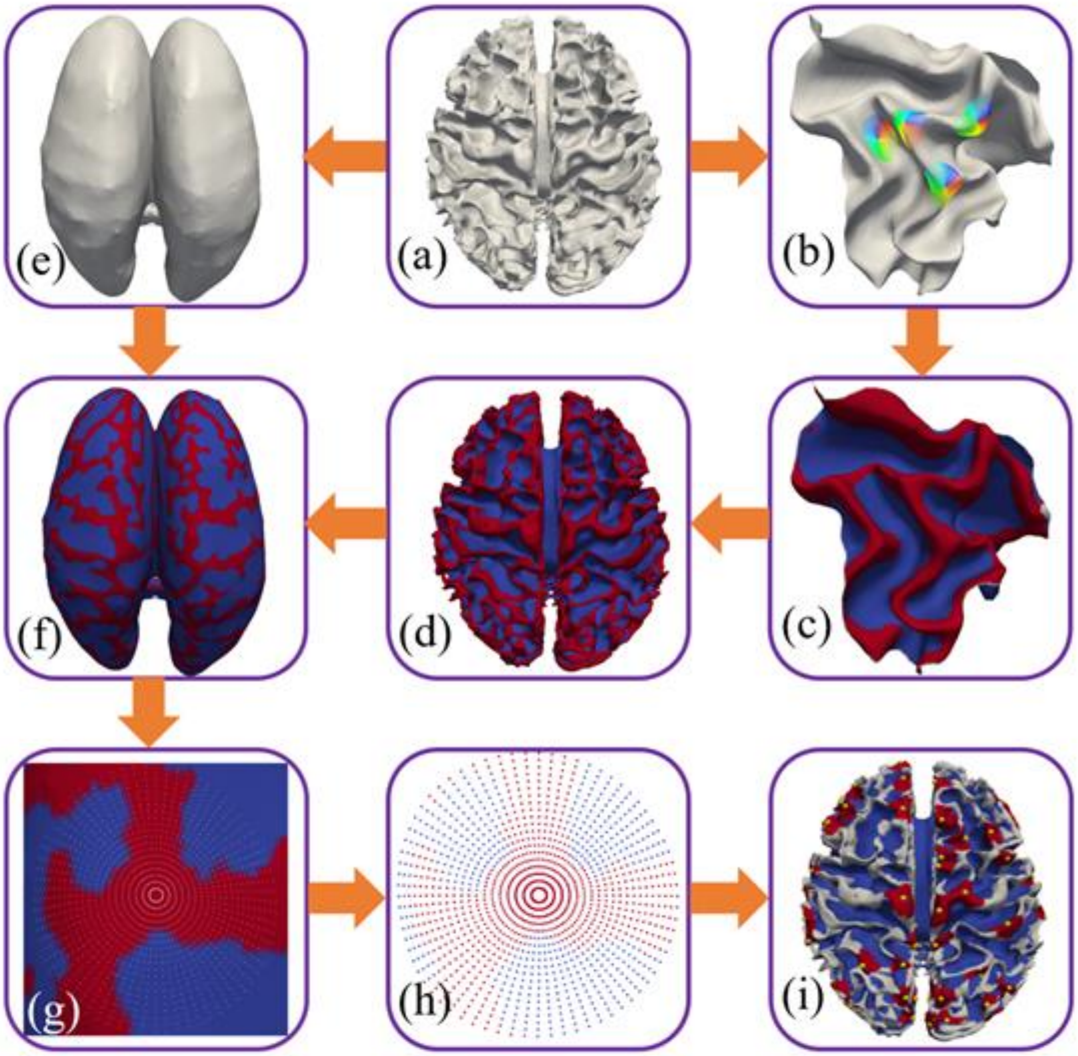

Figure 2.2. Illustration of automatic 3-hinge gyral fold extraction on a human brain. (a) A reconstructed white matter (WM) cortical surface; (b) Profiling every voxel on the surface; (c) Cortical features detected after profiling; (d) The cortical surface profiled by sulcus (blue) or gyrus (red); (e) The corresponding inflated surface which has the same number of points as (a); (f) Mapping the sulcus and gyrus feature on the inflated surface.; (g) Second profile on a sulcus vertex; (h) Profile spokes labeled by sulcus or gyrus; (i) Cortical surface with the detected centers of 3-hinge (red region, center: yellow dots) and 2-hinge area (gray region).

3.4 Fiber density calculation on 2-hinge and 3-hinge gyri

After dividing the gyri vertices into 2-hinge and 3-hinge areas, we then calculated the fiber density on all of the 3 hinges and 2 hinges detected on the cortical surface. Fiber density is defined as the number of DTI-derived streamline fibers per unit surface area [25]. Following this definition, we calculated the fiber density of both 3-hinge gyri and 2-hinge gyri by averaging density values of the surrounding area of each vertex within radius r=2.5mm of its hinge center, the result of which is then used to represent the fiber density of a certain hinge. Radius of 2.5mm is chosen to avoid potential overlapping between 2-hinge gyri and 3-hinge gyri when we perform the averaging calculation. Finally, we made comparisons in fiber density between 2-hinge gyri and 3-hinge gyri in macaques, chimpanzees and human brains. This computational pipeline of measuring fiber densities on 2 hinges and 3 hinges is similar to those used in our prior studies [24, 57].

3.5 Computational model of biomechanical simulations

Three-dimensional (3D) finite element analyses on a double-layer soft tissue model that mimics a small piece of the cortex are performed to investigate the fundamental mechanism of consistent hinge formation in the cortical folding, as illustrated in Figure 2.3(a). The top layer represents the developing cortical plate (cortex) and the bottom layer is the core of the brain which is considered as a simple organization of the subplate, intermediate zone and ventricular zone, as we designed and tested in our prior studies [72]. The cerebral cortex is a thin (2–4 mm) [58] layer in contrast to the inner core which has a thickness around 50 mm [73]. The dimension of the plate is selected to be large enough ($300\times300\times50\text{mm}^3$) in comparison with the wavelength of cortical folds. In Figure 2.3(a), the green area in the middle of the free surface of the cortex layer in the model is an indicator that shows there is a bundle of axonal fibers beneath it. The material properties of the green area are set the same as the cortex, and the main purpose of the green area is to help trace the location of axonal fibers after cortical convolution. Figure 2.3(b) shows the cross-section of the cortex model. The part with blue in the model represents the bundle of axonal fibers which are across the entire core. In this model, we utilize that differential growth in the cortex as the basic driving mechanism for cortical folding, similar to previous simulation studies [74-76] .

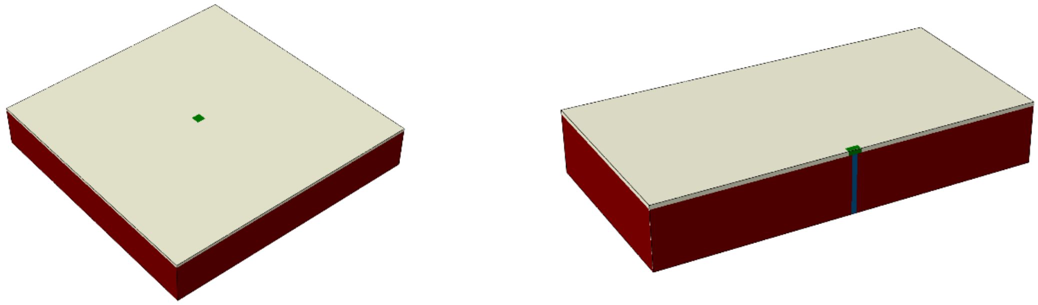

(a) (b)

Figure 2.3. The double-layer soft model mimicking a small piece of the cortex. (a) An entire model with a green area in the middle representing there is a bundle of axonal fibers beneath it; (b) The cross-section of our cortex model. Blue color represents a bundle of axonal fibers.

Growth in this soft tissue model is simulated via thermal expansion [77-79]. For understanding the detail of analogy between volumetric growth model and thermal stress model please check reference [77]. The growth rate of bundle of fibers is considered to be variable to conduct different scenarios, so that we can explore how growth rates of axonal fibers can regulate the formation of consistent gyri and hinge patterns for the green area in our model. Material properties of the cortex and core are set as the same in the model since recent study has shown that there is no significant difference in material property between gray and white matter of the brain [80]. Our previous studies have shown that morphological patterns of the cortex model after growth are independent of the absolute value of elastic modulus of the cortex and core of the cortex, but they depend on the ratio of their moduli [72, 81]. The axonal stiffness depends critically on the degree of myelination may change substantially during development [82]. From other hand, our results showed that stiffness of fibers do not have considerable effect on the gyrification and only their growth ratio show impact. Therefore, in our model, the stiffness of axonal fibers is assumed to be the same as the cortex and core have, and it is set as a constant. All finite element (FE) simulations are carried out by the popular package of ABAQUS.

4. Results

Based on the methods described above, we calculated the fiber densities on 2 hinges and 3 hinges in macaque/chimpanzee/human brains. Comparisons were performed across these three primate species. Examples of the cortical surfaces color-coded by fiber density values are shown in Figure 2.4. We can see that the axonal fibers are much less dense in macaque and chimpanzee brains than that in human brain. Also, the fiber density on gyri is much denser than that on sulci, which is consistent with our previous findings in [24, 57]. The quantitative measurements in Sections 4.1-4.3 are based on the similar computational pipeline described in Section 3.3.

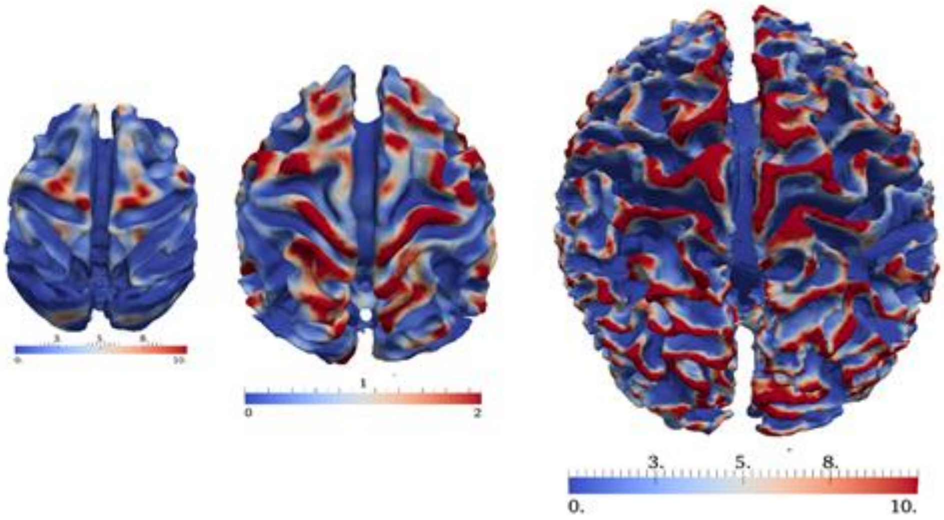

Figure 2.4. Examples of the cortical surfaces color-coded by fiber density values across the three species with the corresponding color bar under each surface (from the left to the right are macaque, chimpanzee and human brain, respectively).

4.1 Fiber density of 2-hinge gyri and 3-hinge gyri in human brains

With the approaches described in Section 3.3, 3-hinge gyri were identified on cortical surfaces reconstructed using DTI data from 64 HCP subjects. Among these human brains, the average number of 3 hinges is around 137. Based on the approach in Section 3.4, we obtained the average fiber densities of 3- hinge gyri and 2-hinge gyri which are 10.1 and 3.85, respectively. This result shows a significant difference in the fiber density between 2-hinge and 3-hinge gyral folds, that is, 3-hinge gyral areas have a larger fiber density of more than 2 times than that on 2-hinge gyral areas, in human brains. Figure 2.5 shows fiber density distribution of 2-hinge gyri and 3-hinge gyri in five randomly-selected human brains, in which yellow spheres are used to locate the centers of 3-hinge gyral areas. Again, it can be seen that axonal fibers connected to 3-hinge gyri are much denser. In addition, the individually average fiber densities on 2 hinges and 3 hinges in Figure 2.6 suggest a large difference between them. Moreover, Figure 2.7

shows the fiber density distribution of 2-hinge and 3-hinge gyri across 64 human brain subjects. It can be noticed that the fiber density range with the largest number of subjects for 2-hinge gyri is 3~4.5 while the range for 3-hinge gyri is 8~11. Statistical two sample t-test (p-value close to 0) also confirmed the significance of such difference among these 64 human brains.

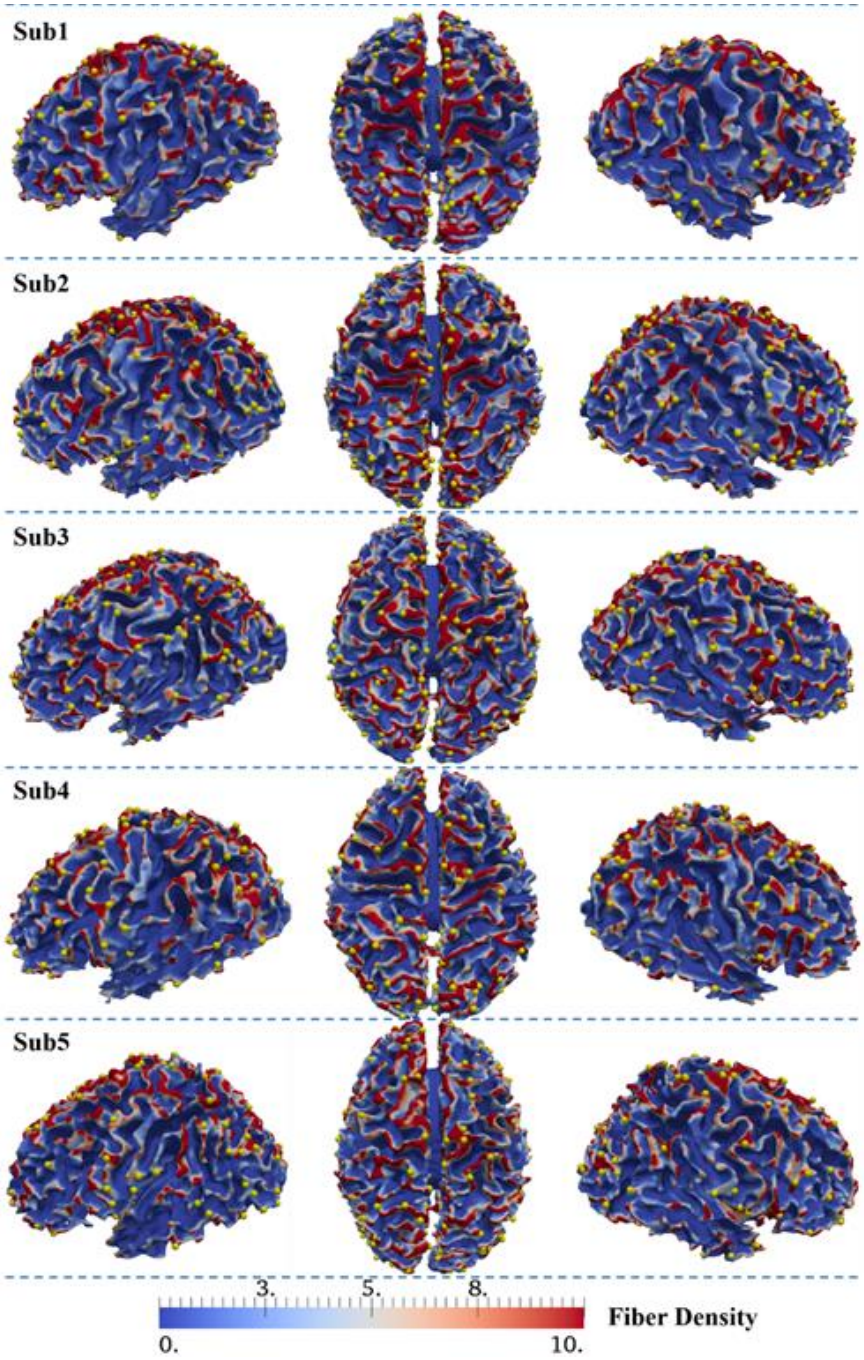

Figure 2.5. Visualization of the distributions of 2-hinge and 3-hinge fiber densities in 5 randomly selected human brains.

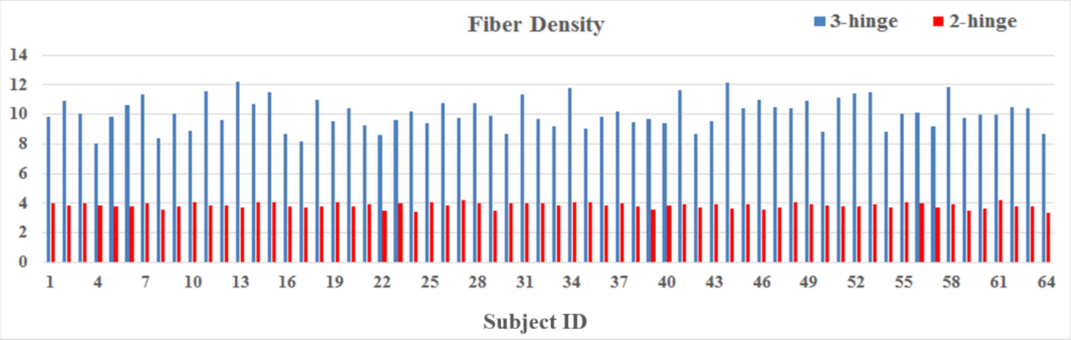

Figure 2.6. The average fiber densities on 2 hinges and 3 hinges within the group of 64 human brains.

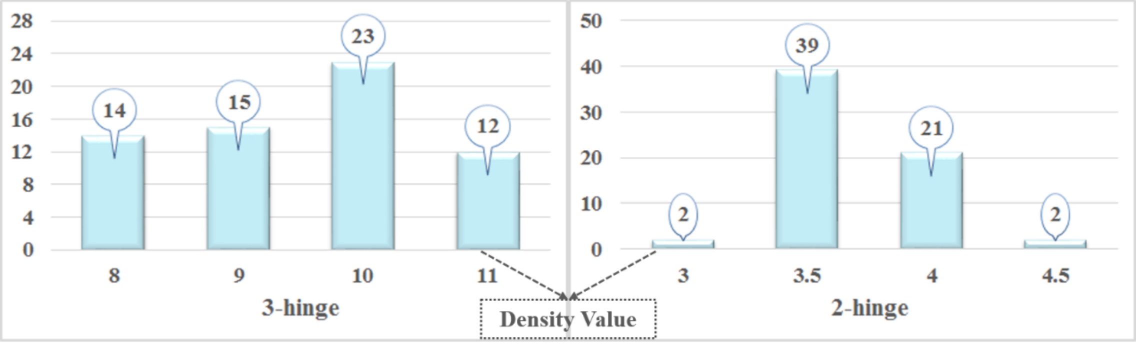

Figure 2.7. 2-hinge and 3-hinge fiber density distributions within the group of 64 human brains. The number of subjects in each range is denoted in the blue circle with an arrow.

4.2 Fiber density of 2-hinge gyri and 3-hinge gyri in chimpanzee and macaque brains

In a similar way, fiber densities in 2-hinge gyri and 3 hinge-gyri in chimpanzee and macaque brains were quantified and shown in Figures 2.8-2.13, respectively. Here, the average fiber densities on 2 hinges and 3 hinges in chimpanzee brains are 0.56 and 1.96, respectively; the average fiber densities on 2 hinges and 3 hinges in macaque brains are 0.92 and 4.95, respectively. From Figure 2.9-2.10 and Figure 2.12-2.13, we can see an even more significant difference between the fiber densities of 2-hinge and 3-hinge gyral folds, that is, the 3-hinge fiber density is more than 2 times larger than that on 2 hinges in chimpanzee brains and more than 4 times larger than that on 2 hinges in macaque brains. Our results show that the fiber density range with the largest number of subjects for 2-hinge gyri is 0.6 ~0.8 while the range for 3-hinge gyri is 2 ~2.5 within the group of 16 chimpanzees. For the group of 20 macaques, the fiber density range with the largest number of subjects for 2-hinge gyri is 1~1.5, while the range for 3-hinge gyri is 4~6. Again, close to 0 p-value derived from two sample t-test performed on the fiber densities on 2 hinges and 3 hinges in the whole brain among all subjects of these two species indicates a very significant difference.

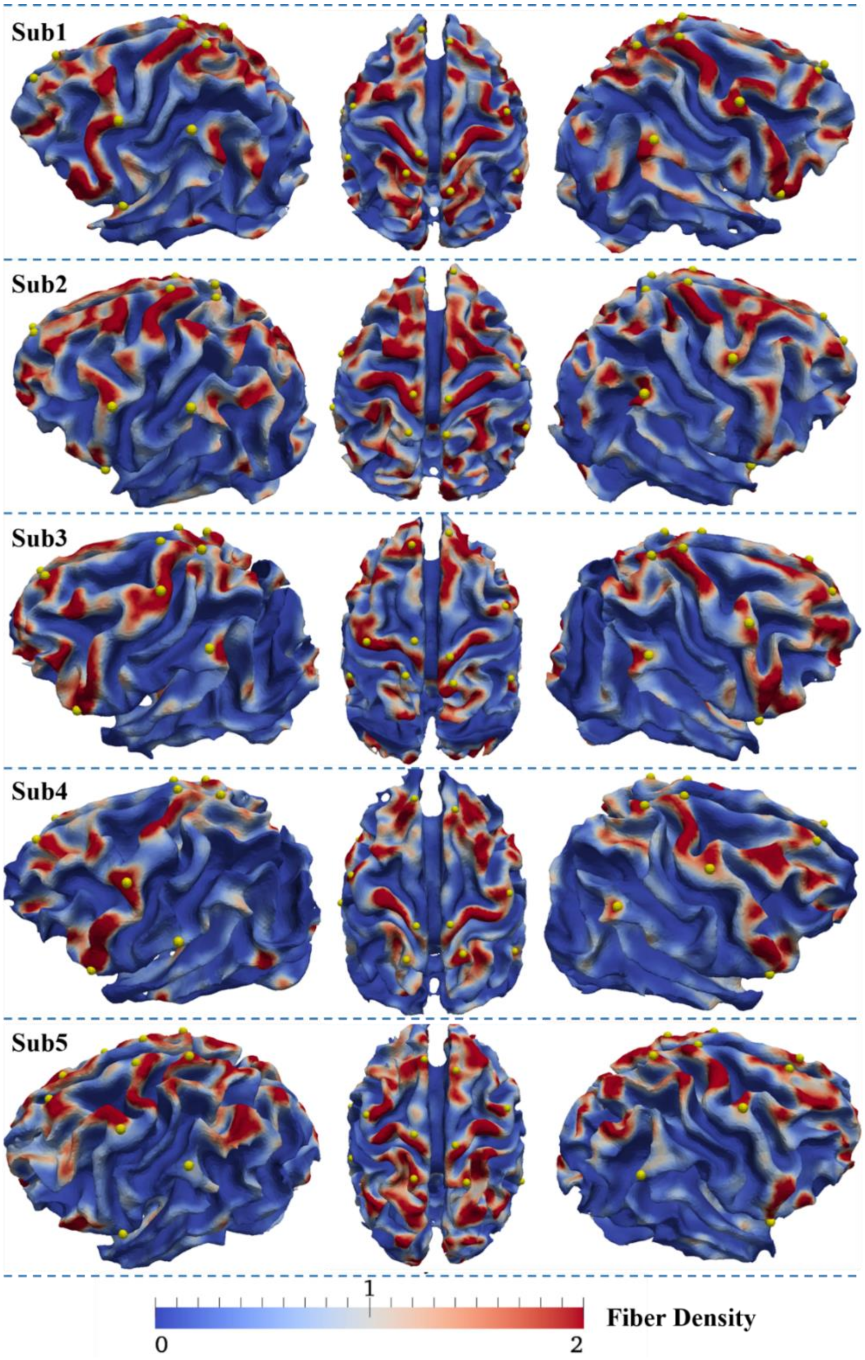

Figure 2.8. Visualization of the distributions of 2-hinge and 3-hinge fiber densities in 5 randomly selected chimpanzee brains.

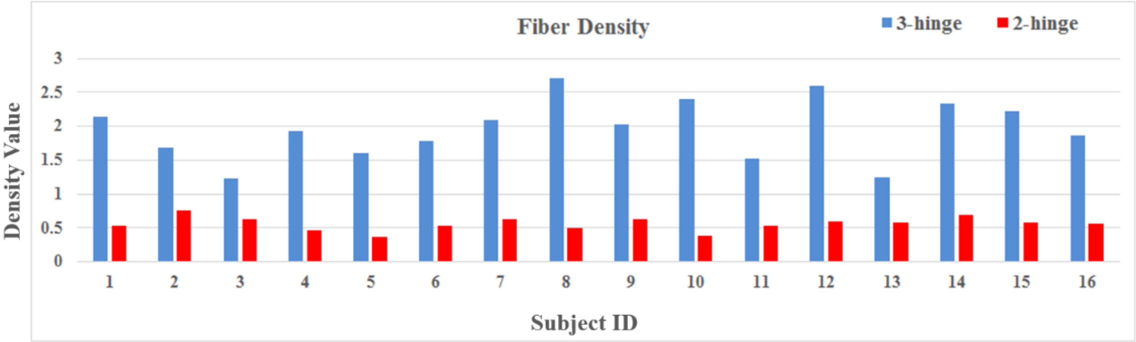

Figure 2.9. The average fiber densities on 2 hinges and 3 hinges within the group of 16 chimpanzees.

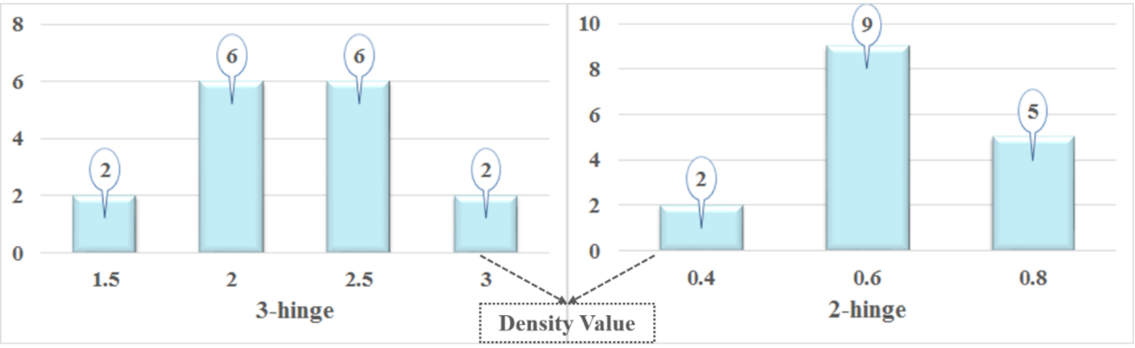

Figure 2.10. 2-hinge and 3-hinge density value distributions within the group of 16 chimpanzees. The number of subjects in each range is indicated in the blue circle with an arrow.

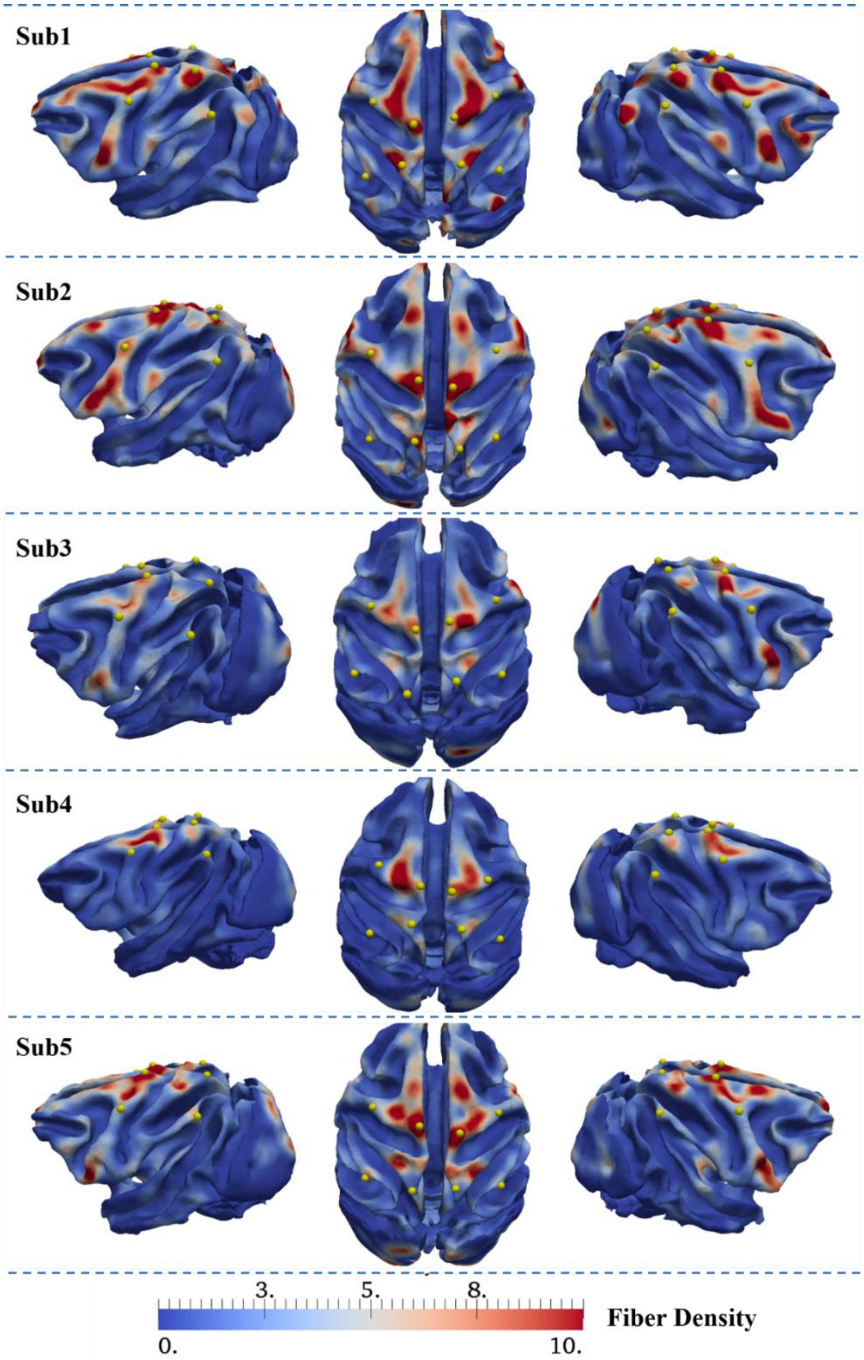

Figure 2.11. Visualization of the distributions of 2-hinge and 3-hinge fiber densities in 5 randomly selected macaque brains.

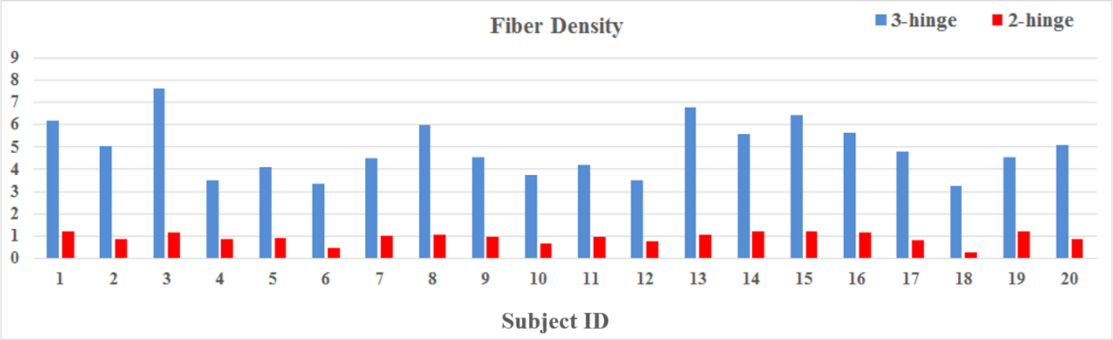

Figure 2.12. The average fiber densities on 2 hinges and 3 hinges within the group of 20 macaques.

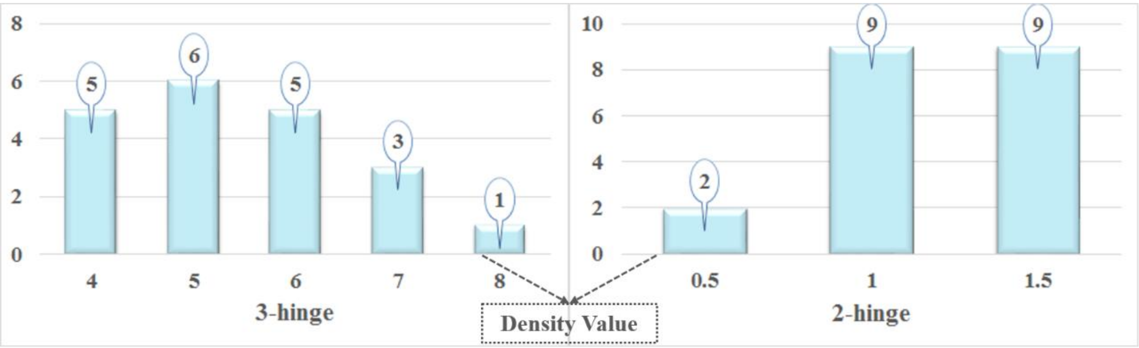

Figure 2.13. 2-hinge and 3-hinge density value distributions within the group of 20 macaques. The number of subjects in each range is indicated in the blue circle with an arrow.

4.3 Correlation between 3-hinge gyral morphology complexity and 3-hinge/2-hinge gyral fiber density ratio across three primate species

From the results in Section 4.1 and 4.2, it can be seen that the ratios of the averaged axonal fiber density on 3 hinges to that on 2 hinges across the whole cortical surface are about 5, 3.5 and 2.5 in macaque, chimpanzee and human brains respectively. Inspired by this observation, we correlate it with the morphology complexity of 3-hinge gyral folds [40] and analyzed the relationship between them. Here, the morphology pattern is referred to as morphology feature combination of a 3-hinge gyrus where each hinge-line corresponds to one of 5 morphology features: ‘I’, ‘V’, ‘U’, ‘S’, ‘O’, detailed in our recent work [40]. Hence, the morphology pattern of each 3 hinge is represented by a combination of three morphology features, such as IVO, IUS and so on. Based on the 33 morphology patterns detected among the three primate species [40], we define morphology pattern complexity for each subject as a ratio of the number of patterns of 3-hinge gyral areas across the whole brain to the total number of patterns 33. Therefore, we can compute morphology pattern complexity of the 3-hinge gyral fold areas for each primate specie and thus derive the mean value for each by averaging them. By analyzing the relationship between 3-hinge morphology pattern complexity and fiber density ratio of 3-hinge to 2-hinge gyri, we noticed that there is an inverse relationship between them across three primate species, that is, the more complex the 3-hinge morphology pattern is, the more likely the fiber density ratio of 3-hinge to 2-hinge gyri will be smaller. The illustration of the inverse correlation tendency is shown in Figure 2.14, in which we can see that from macaque, chimpanzee to human brains, the morphology pattern complexity increase, while the fiber density ratio of 3-hinge to 2-hinge gyri across the whole brain goes down. These interesting observations support our hypothesis that axonal fiber densities might play an important role in regulating the shape formation of 3-hinge gyri, that is, stronger regulations associated with larger fiber density ratios of 3-hinge to 2-hinge induce less 3-hinge morphology complexity and variability.

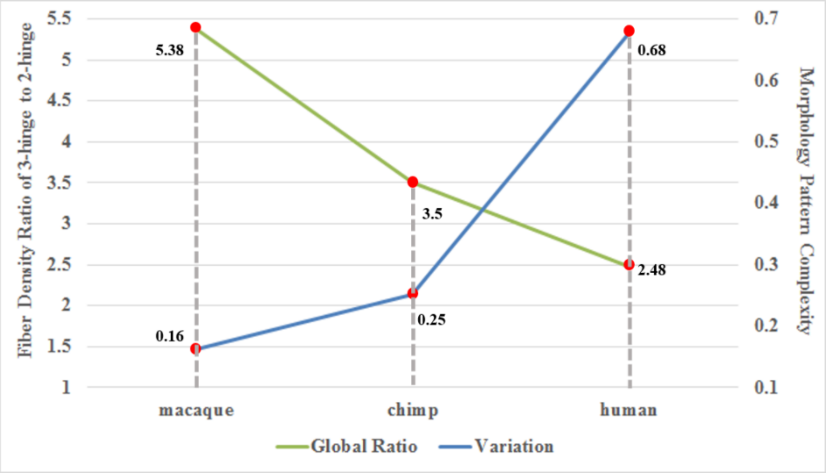

Figure 2.14. Inverse correlation between average fiber density ratio of 3-hinge to 2-hinge gyri and average morphology complexity in macaque, chimpanzee and human brains. The green line is the global fiber density ratio that refers to the vertical axis on the left, and the blue line is the morphology complexity that refers to the vertical axis on the right.

4.4 Computational results

Figure 2.15 shows a dynamic convolution process of a brain model. Both the cortex and axonal fibers in our model are assumed to grow, and after certain growth, our cortex model loses stability and forms the convoluted pattern. As a result, 2-hinge and 3-hinge gyri are observed on the free surface of the cortex. We can also observe that there is a 3-hinge gyrus on top of the axonal fibers in this model. Experimental observations in the literature have revealed that axonal fibers can be either under tension or compression, but the effect of axonal fibers on the formation of consistent gyral hinges remains unanswered [82]. Therefore, by controlling the growth rate of axonal fibers we are able to tune the force status inside fibers and look into the possible explanations on the formation of consistent gyral hinges in areas with high concentration of fibers. Two types of computational models are considered here: one without axonal fibers and the other one with axonal fibers, as detailed in the following two subsections respectively.

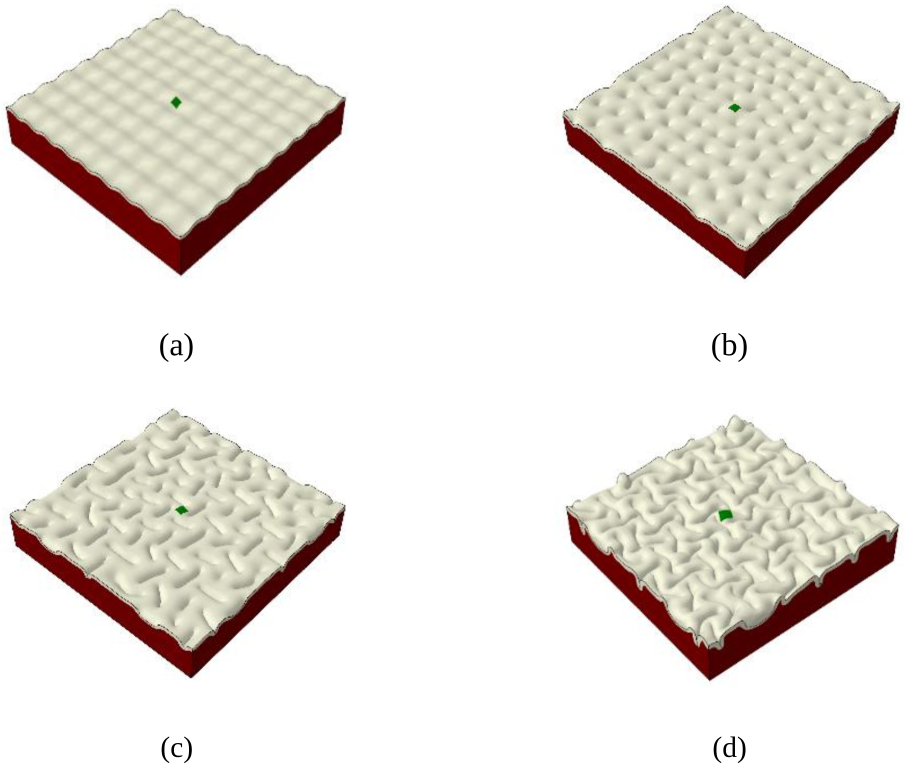

Figure 2.15. Initial perturbation and convolution of the model. (a) Different initial perturbations are applied on the free surface of cortex; (b) Instability initiation; (c) Folding after instability; (d) Convolution of the model. The cortex and fibers are growing simultaneously and create a convoluted pattern on the free surface of the cortex. Growth rate of fibers is the same as the cortex growth rate. The green area is located on a hinge.

4.4.1 Simulation model without fiber

In order to determine the effect of axonal fibers on consistent gyral hinge formation, first, we performed a series of computational simulations only with growth in the cortex and considered them as control studies. Since we have performed and published the similar studies [72], here we just summarizes several key findings in brief. The growth in the cortex without any contribution from axonal fibers can produce convoluted patterns with gyri and sulci as we expect, but the sites of gyral hinge formation in the convoluted model look unpredictable and fairly random. In order to confirm this randomness of gyral hinge sites in our simulation models without axonal fibers, we performed a series of computational simulations with the same model specifications (growth rate, geometric parameters, and materials properties) except the initial small perturbations as shown in Figure 2.15(a). Models with different initial perturbations are hypothesized to mimic the individual brain samples we had in imaging data analyses. These findings suggest that homogeneous growth in the cortex fails to produce consistent gyral hinges on a specific site [72], Combining this simulation result with the imaging data analysis result in Sections 3.1-3.3 that much denser fibers are connected to gyri in comparison with sulci, it is reasonable to hypothesize that denser fiber connections induce or regulate the formation of gyral hinges, including 3-hinge gyri.

4.4.2 Simulation model with fibers

Following the control study, we performed another set of simulations to test our hypothesis that the presence of axonal fibers as well as their growth in our cortex model can regulate or determine the sites of gyral hinge formation. By adjusting the growth rate of axonal fibers in our model we can screen through various scenarios to possibly find the right parameters which can produce gyral hinges on top of the axonal fibers. Here, the growth rate of axonal fibers is mimicked by a dimensionless number according to the growth rate of the cortex. Figure 2.15(d) shows the result of a model with growing axonal fibers. The growth rate of axonal fibers is set the same as the cortex. It can be seen that on top of growing axonal fibers a 3-hinge gyrus is formed. An interesting question arises: how does the presence of the growing axonal fibers influence the sites of gyral hinge formation where all other parameters are kept intact in our model, e.g. growth rate of the cortex and mesh size of the computational model?

In order to answer the abovementioned question, we run a considerable amount of finite element simulation cases with different growth rates in axonal fibers. We set the growth rate of axonal fibers as five different values, all of which are comparable with the growth rate in the cortex. Within models with the same growth rate of axonal fibers, different initial perturbations are hypothesized to mimic the individual brain samples we had in imaging data analyses. Table 2.1 collects the folding patterns of the green area in our model (Figure 2.15) after running multiple cases with and without fibers. Results show that there is a very high possibility to form a 3-hinge gyrus in the specific area when the growth rate of axonal fibers is close to the growth rate of the cortex, while the green area in models without axonal fibers could be located on hinge, sulci or in-between banks.

Table 2.1. Statistical results of the numbers of the locations of the special areas on gyral hinges, sulci and in-between banks.

	Model with fibers (growth rate of fibers/growth rate of cortex)					Model without fibers
	0.7	**0.8**	**0.9**	**1**	**1.1**	
hinge	4	7	9	10	10	14
sulci	0	0	0	0	0	19
banks	6	3	1	0	0	17
total	10	10	10	10	10	50

Our results show that a higher growth rate in axonal fibers always leads to 3-hinge gyri formation on top of the axonal fiber bundle. Therefore, our findings imply that the presence of growing axonal fibers could be responsible for forming a consistent gyral hinge in a special area with a higher concentration of axonal fibers. Interestingly, Table 2.1 also shows that the sites with a high density of growing axonal fibers do not develop any sulci as we observe in experimental results. Figure 2.16 shows three different initial perturbations in our model with the presence of growing axonal fibers generally leading to the formation of different hinge patterns, but in all cases the green area always develops a 3-hinge gyrus. These 3-hinge patterns in Figure 2.16 are comparable with experimental 3-hinge patterns like IVO and IUS observed in neuroimaging data. This observation is in good agreement with our experimental observation in individual brain samples and demonstrates the regulating effect of dense growing axonal fibers in the consistent gyral hinges, particularly 3-hinge formation.

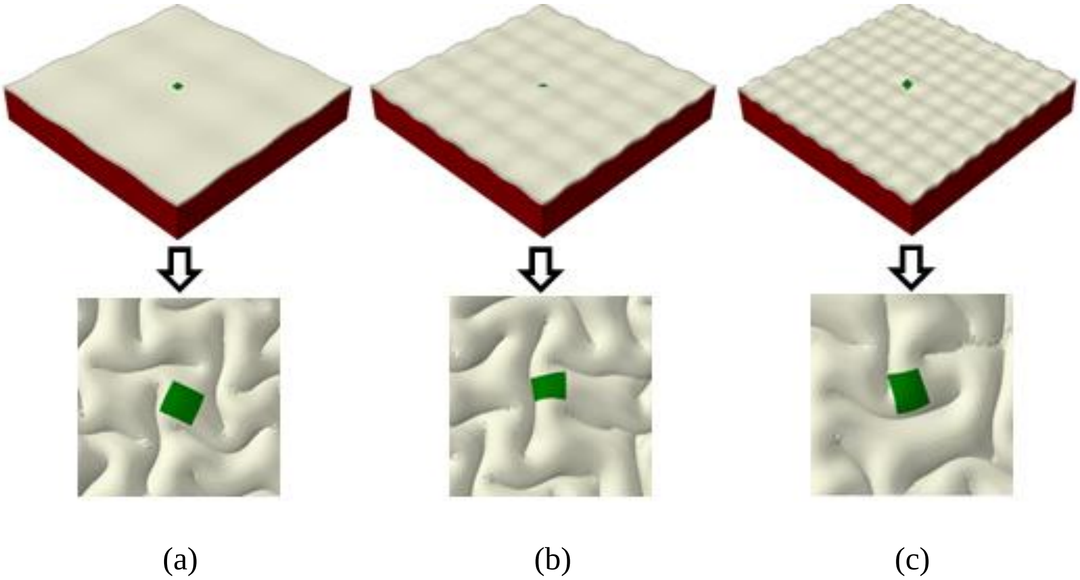

Figure 2.16. (a)-(c) Three different initial perturbations after convolution lead to different hinge patterns in the center of the model. In all models with the presence of the growing fibers, the green area is located on a 3-hinge.

4.4.3 Scattered and different shapes of fibers

The main objective of our simplified model was to demonstrate that 3-hinge gyrus can consistently form in a special area with a high density of fibers. We know that in a real brain there are many complex fibers with various types and orientations. Incorporating such complexity into the mechanical model is very challenging at this stage. Therefore, by a simplified model, we are able to incorporate mechanical effect of growing fibers on the formation of 3-hinges. Since we selected a small patch of the entire cortex, therefore it is acceptable to assume that the orientation of fibers is perpendicular to the cortex. In a bigger scale, the type and orientation of fibers can be different across the entire cortex. Here, we focused our study on a single fiber bundle and its counterpart 3-hinge.

In the next step, we increased the number of fiber bundles and placed them randomly in our model. Simulation results, again, confirmed our hypothesis that 3-hinges were always formed at sites where the growing fiber bundles were embedded underneath. Figure 2.17 shows the evolution steps of a finite element model with ten scattered growing fiber bundles.

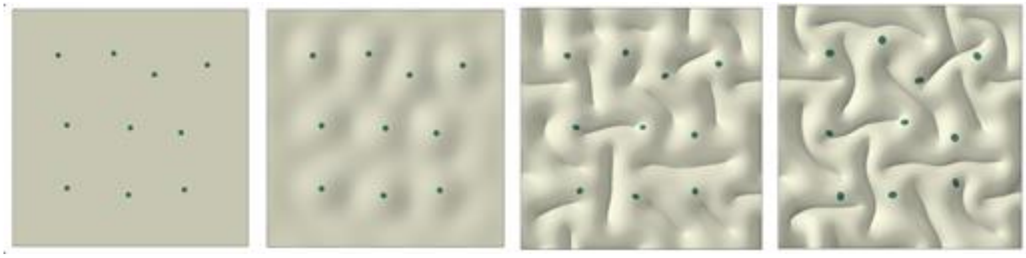

(a) (b) (c) (d)

Figure 2.17. (a)-(d) Evolution steps of a finite element model with ten growing fiber bundles. After convolution, 3- hinges were always formed on the top of these growing fiber bundles.

Figure 2.18 shows comparison of two finite element models with a real brain image. Initial location of fibers was set roughly according to the location of 3-hinges from the image data. Initial perturbations were applied on the free surface of FE models. It is clear, after growth and gyrification, that locations of 3-hinges on the free surface of the cortex are the same as the counterparts on the real brain. We speculate the discrepancy between gyri and sulci patterns in the FE models and real brain is due to the effect of 2-hinges fibers which have not been included in the FE models. This issue is not the scope of our study at this stage.

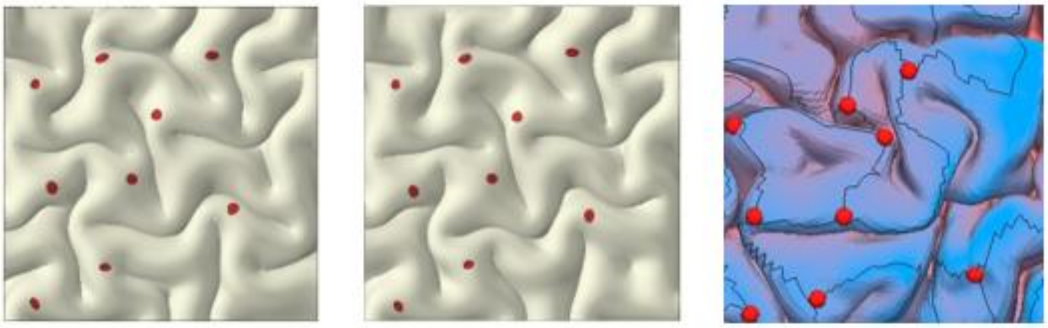

(a) (b) (c)

Figure 2.18. Contribution of fibers growth on the convolution morphology. (a) Finite element model # 1; (b) Finite element model # 2; (c) A small patch of a real brain with 3-hinges. Red dots in three figures means 3-hinges.

In order to better represent the realistic fiber growth in brain, we incorporated a gradient growth in a special type of 3-hinges. Since the density of fibers in the junction of 3-hinge lines (red points in Figure 2.18(c)) is higher than those along lines (solid lines in Figure 2.18(c)), therefore we constructed a complex FE model to incorporate this growth difference in a fiber bundle. This model allows us to set a high growth ratio in the junction of the 3-hinge and lower the growth ratio along the connecting lines to zero at the tip of lines. In other words, the growth ratio is the highest at the junction of 3-hinge and is zero at the tip of connecting lines, as shown in Figure 2.19(a). We created several models with and without growing fiber with gradient growth to check the contribution of fibers on the formation of 3- hinges. Results, again, showed that without growth of fibers, 3-hinges might form in random locations (Figure 2.19(b)). It is clear, in the bottom row of Figure 2.19(b) Y- shaped red area can acquire different shapes, since there is no growing fiber beneath them. In contrast, in the top row of Figure 2.19(b) Y-shaped red area always forms Y-shaped 3-hinges because there are growing fibers beneath these red areas.

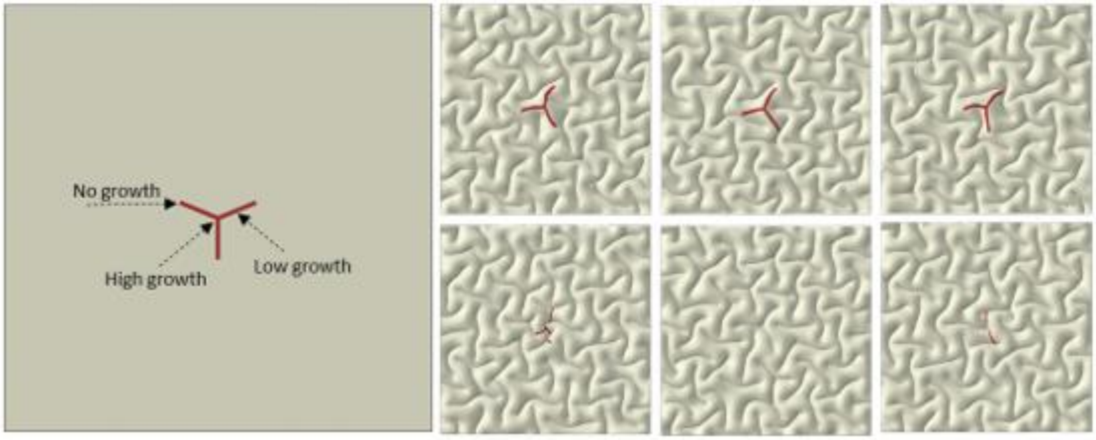

(a) (b)

Figure 2.19. Effect of gradient growth of Y-shaped fibers on the formation of 3-hinges. (a) the initial computational model. (b) the top row: models with growing fibers; the bottom row: models without growing fibers.

Finally, we added several similar “Y” shape fibers into the computational model. Figure 2.20(a) shows the initial computational configuration and Figure 2.20(b) shows the model after growth and cortical convolution. It can be seen that growing fibers are able to control the location and type of the 3-hinges. If other shapes of fibers are implemented in the computational model, different kinds of 3-hinges after convolution are accessible. It is noteworthy to mention that the red “Y” shape areas on the cortex, are indicators that show there are the same shape of fiber bundles beneath them. The material properties of the red areas are set the same as the cortex, and the main purpose of the red areas are to help trace the location of axonal fibers after cortical convolution.

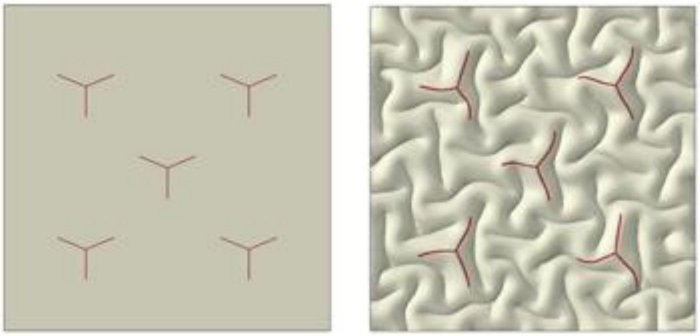
(a) (b)

Figure 2.20. (a) Top view of "Y" shape fibers with gradient growth in initial state; (b) Top view of the model after growth and convolution. Growth ratio linearly decreases from the intersection point of hinges lines to the tip of them.

5. Discussion and Conclusion

As far as we know, most of previous major stream descriptors for cortical folding patterns focus on cortical complexity quantification, which are difficult to quantify the variation of folding patterns and infer anatomical correspondence of the cortical landscapes based on exclusively local-scale or global-scale descriptors. However, the descriptor proposed in our work (2-hinge and 3-hinge) took the advantages of both parametric and surface profiling methods to analyze cortical folding patterns in terms of gyral hinge numbers and shapes. Previous works have shown that the axonal fibers connected to gyri are significantly denser than those connected to the sulci in human, chimpanzee and macaque brains [57], which offers a novel explanation into the intrinsic relationship between cortical folding and axonal wiring. In this study, we further quantitatively measured the fiber densities of 2-hinge and 3-hinge gyral areas in macaque, chimpanzee and human brains and quantitatively compared them within each species, which is a great piece of enhancement compared with the previous ones. Our results overwhelmingly showed that fiber densities in 3-hinge gyri are much higher than those in 2-hinge gyri, and thus we are strongly motivated to hypothesize that besides cortical expansion as the primary mechanism of gyrification, denser fiber connections can also induce the formation of 3-hinge gyri. In order to examine the biomechanical basis of this hypothesis, we designed 3D finite element soft tissue models and performed extensive computational simulations with a variety of settings to investigate the fundamental biomechanical mechanism of consistent 3-hinge formation. Our simulation consistently results showed that gyral regions with higher concentrations of growing axonal fibers have much higher probability of forming 3-hinge gyri. Altogether, our integrated studies of neuroimaging data analyses and computational biomechanical simulations offer a plausible theory of 3-hinge gyri formation: denser growing fiber connections induce 3-hinge gyri formation.

Given the strong correlation between brain structure and function, e.g., strong structural connectivity predicts functional connectivity (Honey et al., 2009; Deng et al., 2014), complex functional regions locate significantly more on gyral regions than sulcal regions and the most complex ones are usually found in 3-hinge area based on a statistical analysis [18], our future work will explore the functional implications that much stronger axonal fibers are connected to 3-hinge gyri in comparison with 2-hinge gyri. For instance, our prior studies have suggested a functional model of cortical gyri and sulci (Deng et al., 2014), that is, gyri are the functional integration centers while sulci are the local information process units. Following this research line, we will further refine this functional model by differentiating cortical 3-hinge gyri and 2-hinge gyri and strive to characterize the possible different functional roles played by 3-hinge and 2-hinge gyral regions, which also can be extended to investigate a variety of neurodevelopmental diseases. The elucidation of the possible functional role differences of 3-hinge and 2-hinge gyri could potentially fundamentally advance our understanding of the structural and functional brain architectures, as well as their relationships.

CHAPTER 3

EXPLORING INTRINSIC FUNCTIONAL DIFFERENCES OF GYRI, SULCI AND 2-HINGE, 3-HINGE JOINTS ON CEREBRAL CORTEX[2]

---

[2] Fangfei Ge, Shu Zhang, Heng Huang, Xi Jiang, Qinglin Dong, Lei Guo, Xianqiao Wang and Tianming Liu. "Explore Intrinsic Functional Differences of Gyri, Sulci and 2-hinge, 3-hinge Joints on Cerebral Cortex." In Biomedical Imaging (ISBI), 2019 IEEE 16th International Symposium, in press. IEEE.
Reprinted here with permission of the publisher.

1. Abstract

Motivated by the unique structural characteristic of 3-hinge gyral joints, in this chapter, I investigate the intrinsic functional differences between gyral, sulcal and 2-hinge and 3-hinge rsfMRI signals from the functional perspective using the most commonly used supervised deep learning model — 1D-CNN (Convolutional Neural Network).

The human cerebral cortex has been commonly known as a highly-folded region which consists of convex gyri and concave sulci. Many previous studies have already revealed the fundamental differences of these convex and concave areas by analyzing structural and functional connectivity patterns. However, to our best knowledge, rare work has been done to explore their intrinsic functional differences from the perspective of neural activity, especially for 3-hinge gyral folding joints. Inspired by current evidences, in this chapter, experiments based on classification models learned by convolutional neural network (CNN) were designed and performed on resting state functional magnetic resonance imaging (rs-fMRI) data of both healthy controls and autism patients from the publicly available ABIDE II database. In our work, gyral and sulcal, 2-hinge and 3-hinge joint rs-fMRI signals were modeled and predicted using CNNs with an average testing classification accuracy of 94.24% for controls, 95.24% for patients and 87.53% for controls, 87.72% for patients at individual level separately, which confirms different functional roles of neural activities under resting state in gyri and sulci, as well as 2-hinge and 3-hinge gyral folding joints in healthy subjects and autism groups. Besides, further analyses on learned characteristic features to differentiate

gyral/sulcal, 2-hinge/3-hinge joint rs-fMRI signals were also designed and performed to interpret our findings.

2. Background and Motivation

The human cerebral cortex is a highly convoluted region which folds itself into gyri and sulci during brain development [3, 4, 43, 45, 83]. Neuroscientific studies have demonstrated that neural structures of concave sulci and convex gyri emerge from a complex cortical folding process which has a close relationship with various factors, such as neurodevelopment[27, 36, 48, 84], cytoarchitecture [4, 51] and cognitive functioning [52-55]. The concepts of folds and folding were originated from folding pattern analysis of rocks in geology [85], which inspires a novel way to describe gyral folding patterns in terms of gyral hinge numbers by taking advantages of both parametric and surface profiling methods [8, 40, 86]. Specifically, 3-hinge gyral joint is a cortical gyral region where 3 different gyral crests meet [8, 86]. Many previous literatures have put much effort in studying differences in gyri and sulci, 2-hinge and 3-hinge gyral joints by analyzing both structural and functional connectivity patterns [15, 24, 26, 86]. However, the intrinsically different functional roles of gyri/sulci or 2-hinge/3-hinge joints in terms of neural activity under resting state have rarely been noticed and explored even for healthy people. For example, the relationship between cortical folding and axonal wiring was studied and it demonstrated that gyri have significantly higher axonal connections relative to sulci, suggesting an axonal pushing mechanism of cortical folding, which have provided a novel insight on fundamental mechanisms for the organization and development of the cerebral cortex [24, 26, 29]. In addition to the analyses of gyri and sulci, a recent investigation into structural and functional cortical architectures is also provided by comparing the DTI-derived fiber densities in 3-hinge and 2-hinge gyral joint regions [86]. Meanwhile, previous efforts were also made to study gyral and sulcal differences from the functional perspective [15, 18, 19, 30]. For instance, it demonstrated that gyri are functional connection centers to exchange information among remote structurally connected gyri and neighboring sulci, while sulci communicate directly with their neighboring gyri and indirectly with other cortical regions through gyri [15]. Based on these abovementioned evidences, we can find that there do exist functional difference when it comes to gyri and sulci.

Thanks to the advancements in machine learning and data mining field during recent years, deep learning techniques has achieved promising performance on image classification, text classification and object detection by using various deep learning models, especially for models based on CNN [87-92]. Nowadays, applications of deep learning to medical image analysis such as disorder classification, image segmentation, registration, lesion detection and so on has also grown rapidly [93-97]. Particularly, we noticed that some CNN models have already been applied on certain brain network analyses based on fMRI data. For example, a 3D CNN framework was proposed to classify and recognize large scale functional brain networks derived from fMRI scans automatically [95] and this framework was improved later in an iterative way which has a more powerful spatial pattern modelling capability [97]. Besides brain network related studies, another recently developed model based on CNN which is deep convolutional auto-encoder (DCAE) was also developed to model task-based fMRI (tfMRI) data by learning discriminative features from tfMRI time series [96].

Considering the promising results achieved by these fMRI studies based on deep learning algorithms and the powerful capability in learning discriminative features of CNN models, we are inspired to apply 1D-CNN classification models to differentiate rs-fMRI time series of gyri/sulci, 2-hinge/3-hinge joints and analyze the learned characteristic features in frequency domain which serves as an important aspect in understanding brain functional characteristics [98-102]. Here, the designed 1D-CNN classification models are applied on rs-fMRI datasets from two institutions of publicly available ABIDE II database, including both healthy controls and autism patients. Our experimental results showed that gyral/sulcal and 2-hinge/3-hinge joint rs-fMRI signals can be differentiated and classified in both healthy subjects and autism groups across scans from different institutions at individual level. In terms of average classification accuracy based on testing data, the promising result which is 94.24% for controls, 95.24% for patients in differentiating gyri and sulci fMRI signals, 87.53% for controls, 87.72% for patients in differentiating 2-hinge and 3-hinge fMRI joint signals does confirm different functional roles of gyri and sulci or 2-hinge and 3-hinge joints in both healthy and autism subjects. In addition, further analyses on learned features in frequency domain also suggested characteristic frequency features of gyral/sulcal and 2-hinge/3-hinge joints. We can observe different frequency distribution patterns of features learned from gyri/sulci or 2-hinge/3-hinge joint rs-fMRI signals which indicated their functional differences as well. In general, our overall results potentially demonstrated the intrinsically different functional roles of gyri/sulci or 2-hinge/3-hinge joints on cerebral cortex which provides a new insight into learning their complex functions.

3. Methods

3.1 Overview

In general, the overall analysis framework based on 1D-CNN classification model can be summarized as follows: We firstly identified the exact anatomical locations of gyri, sulci, 2-hinge, 3-hinge joints on the cortical surface individually. Then, according to the correspondence between voxels in the registered fMRI volume and vertices on the cortical surface from the same subject, different types of fMRI signals (gyri, sulci, 2-hinge, 3-hinge) can be extracted. After that, either gyri/sulci fMRI signals with label 0 (sulcus) and 1 (gyrus) or 2-hinge/3-hinge fMRI signals with label 0 (2-hinge) and 1 (3-hinge) of each single subject were rearranged together and used as sample signals for both training and testing purpose in 1D-CNN classification model. In this way, each subject comes with two classification models, one is for gyri/sulci fMRI signal differentiation, the other is for 2-hinge/3-hinge fMRI signal differentiation. Finally, we did a further analysis on the characteristic features learned from 1D-CNN models and tried to interpret them in frequency domain. The illustration of the whole analysis pipeline can be learned from the following sections.

3.2 Data description and preprocessing

In this study, our experimental data were downloaded from the publicly available database ABIDE II (Autism Brain Imaging Data Exchange II). Dataset from two institutions (BNI: Barrow Neurological Institute and EMC: Erasmus University Medical Center Rotterdam) are chosen as a test bed. According to manually checked preprocessing results, 58 subjects (29 control, 29 patients) from BNI and 51 subjects (27 controls, 24 patients) from EMC are considered as high quality and thus selected. Please visit http://fcon_1000.projects.nitrc.org/indi/abide/abide_II.html for detailed acquisition parameters information.

Preprocessing for T1-weighted MRI data included image resampling, skull removal, tissue segmentation and cortical surface reconstruction. Specifically, T1 images were resampled into 1mm isotropic images using spline interpolation. For rs-fMRI data, skull removal, motion correction, spatial smoothing, temporal pre-whitening, slice time correction, global drift removal, band-pass filtering, and linear registration to their individual MRI space were performed. Here, the registration step can guarantee the correspondence between voxels in rs-fMRI volume and vertices on cortical surface. In this way, different types of fMRI signals (gyri, sulci, 2-hinge, 3-hinge) can be extracted according to their anatomical labels. In this work, all the preprocessing steps were implemented by using FSL (https://fsl.fmrib.ox.ac.uk/fsl/fslwiki/) [70] and other tools based on Freesurfer (http://surfer.nmr.mgh.harvard.edu/) [71].

3.3 rs-fMRI signal extraction

In order to prepare rs-fMRI time series samples for 1D-CNN model training and evaluation, we first need to separate gyral/sulcal and 2-hinge/3-hinge gyral joint areas and extract the corresponding rs-fMRI signals. Since our classification model was trained at individual level, all rs-fMRI data need to be registered to their individual MRI data space to ensure the correspondence between rs-fMRI volume and cortical surface. Here, one of the attributes of the reconstructed cortical surface generated from FreeSurfer named ‘sulc’ is used to separate gyral/sulcal regions. A ‘sulc vector’ corresponding to all the vertices on the cortex comes with each cortical surface, the value of which refers to sulcal depth. Here, the sulcal depth is the opposite measurement term to gyral altitude which means sulcus with positive sulci depth will have a corresponding negative gyral altitude, gyrus with negative sulci depth will have a corresponding positive gyral altitude and vice versa. Specifically, gyral altitude is defined as the dot product of the movement vector during inflation with the surface normal which can be viewed as the altitude from the current vertex to the “mid-surface” that exists between gyri and sulci [5, 32]. Therefore, if the value of ‘sulc’ for a single vertex is greater than 0, then it will be labelled as a sulcal vertex; otherwise, it will be labelled as a gyral vertex. However, the correctness of vertex labeling of vertices at the boundary of gyri and sulci areas is sometimes not assured. In such case, we choose another reliable threshold of 0.3 instead. That is, vertices with ‘sulc’ value greater than 0.3 belong to sulcal areas and vertices with ‘sulc’ value less than -0.3 belong to gyral areas. In this way, the only influence resulted from the newly set threshold 0.3 is that we may have less gyral/sulcal rs-fMRI sample signals, but all the samples are guaranteed with the right labels. At the same time, the number of sample signals after applying threshold 0.3 is still large enough for training purpose as can be seen in Section 3.4. Once the extraction of gyral regions completed, the separation of 2-hinge/3-hinge gyral joint areas could be performed next. In this chapter, 3-hinge center vertices were extracted automatically based on a novel computational framework which can construct gyral nets from surface meshes efficiently. Here, ‘gyral net’ was proposed as a new representation of cortical gyri/sulci organization pattern and modeled cortical architecture from a graph perspective. For the details of this automatic framework in extracting 3-hinge gyral joints, please refer to [32].

As shown in Figure 3.1, we can see yellow gyral nets [32] as well as red 3-hinge center vertices across the whole cortical surface. To better visualize, we select two representative three hinge areas of both left and right hemispheres which are circled by dashed blue line and zoomed in. From the enlarged part, it can be seen clearly that 3-hinge gyral region is a cortical gyral joint where 3 different gyral crests (highlighted green lines) meet. To separate 2-hinge and 3-hinge gyral regions, a radius of 6mm is predefined which indicates that the surrounding areas of each vertex within radius r=6mm of its 3-hinge center are labelled as 3-hinge gyral regions, and areas consisting of the remaining vertices on gyral regions are all labelled as 2-hinge gyral regions. Consequently, the separation of gyral/sulcal and 2-hinge/3-hinge areas can be visualized in Figure 3.2 and the rs-fMRI signals with different labels can be extracted by mapping the vertices on cortical surface to voxels in rs-fMRI volume data individually. Here, the radius of 6mm is chosen empirically, it looks reasonable and can be visualized from the right column in Figure 3.2. Moreover, such a radius can also ensure the sample size of 2-hinge and 3-hinge rs-fMRI signals comparable for the training and testing process in the classification model. We can see that the left column in Figure 3.2 shows the left and right hemisphere cortical surface parcellation measured by sulcal depth, it can be observed that gyral region corresponds to a negative ‘sulc’ value and sulcal region corresponds to a positive ‘sulcal’ value. For the middle column in Figure 3.2, gyral region by red and sulcal region by blue under the threshold 0.3 can be visualized, some of the remaining areas may belong to gyral or sulcal region, but in order to ensure the correctness of the extraction of different types of fMRI signals, we choose to not consider the vertices at the boundary. From the right column, we can see the corresponding 2-hinge (red) region and 3-hinge (green) region constrained by radius=6mm and it can be found that the range of 3-hinge areas under such radius constrain is quite reasonable.

Once the anatomical labels (gyri, sulci, 2-hinge,3-hinge) of rs-fMRI signals were confirmed, they can be extracted accordingly and served as training and testing samples in 1D-CNN model.

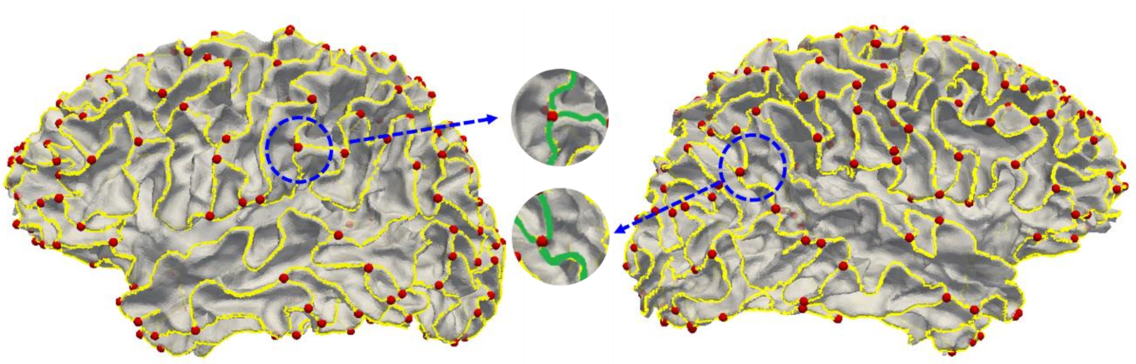

Figure 3.1. Visualization of gyral net (yellow lines) and 3-hinge center vertices (red dots). In the middle, there are two enlarged representative 3-hinge joints highlighted by green lines (3-hinge joint is where 3 different gyral crests meet) from both left and right hemisphere. The corresponding region of the 3-hinge joints in both hemispheres are dashed by the blue circle on the cortical surface.

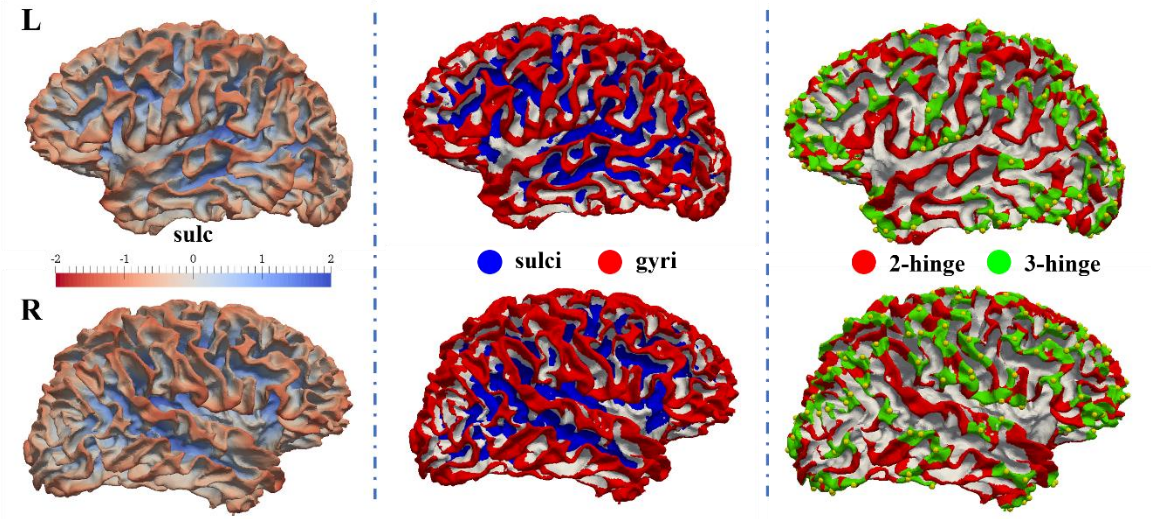

Figure 3.2. Region separation. Left: original cortical surface parcellation measured by sulcal depth. Here, gyral region has a negative depth value and sulcal region has a positvie depth value. Middle: sulcal/gyral region separation under 'sulc' threshold thr=0.3. Sulcal region (blue) corresponds to 'sulc'>0.3 and gyral region (red) corresponds to 'sulc' < -0.3. Vertices at the boundary won't be considered and are left as gray. Right: 2-hinge (red)/3-hinge (green) region separation under radius r=6mm, 3-hinge center vertices are represented by yellow dots.

3.4 1D-CNN classification model architecture

In our work, the architecture of 1D-CNN classification model is shared by all sets of training samples to differentiate either 1D gyral/sulcal or 2hinge/3hinge rs-fMRI time series. One key reason that we performed the classification based on CNN method is because CNN models do not require features completely designed and extracted by humans in advance but can instead learn increasingly higher level features during the training process. Here, our simple but effective model is composed of alternate convolutional and pooling layers and subsequently with a global average (GA) pooling layer, then a fully connected (Dense) layer to perform classification in the end as shown in Figure 3.3. The red dot in Dense layer can either represent gyri in gyri/sulci classification or 3-hinge in 3-hinge/2-hinge classification and the blue dot can either represent sulci or 2-hinge in the same way. Specifically, we adopted a GA layer instead of a conventional fully connected layer right after the last pooling layer and the reasons behind this are two folds: Firstly, it can minimize overfitting by reducing the total number of trainable parameters in the model. In this case, the GA layer reduce each input feature map to a single number. Secondly, GA layer enforced a one-by-one correspondence between the filters in the last convolutional layer and the softmax weights (blue and red weight lines in Figure 3.3) connecting GA and Dense layer. Once the correspondence is established, we can further exploit class specific characteristic features learned from our CNN models [103]. Through the GA layer, the feature map of each filter connected to the two neurons in the output layer (Dense) with two labels (gyri/sulci or 2-hinge/3-hinge).

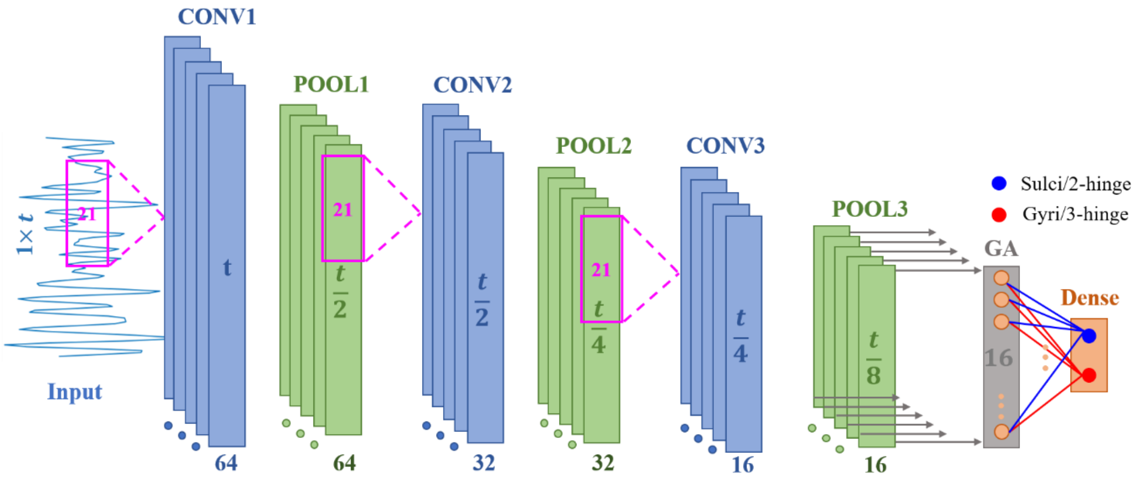

Figure 3.3. The architecture of 1D-CNN classification model. CONV is short for convolutional layer, POOL is short for max pooling layer, GA stands for global average pooling layer and Dense layer is the final layer to output classification result containing two labels (gyri/sulci or 3-hinge/2-hinge). Here, the length of the input original rs-fMRI time series is represented by t and the length of filter is fixed as 21. Filter numbers for three convolutional layers are 64, 32, 16 separately. Particularly, a one-by-one correspondence exists between the filters in the last convolutional layer and the softmax weights.

All the implementations are based on Keras with a backend of TensorFlow. The hyperparameter settings of our proposed classification model are as follows. Filter length is set as 21 which is defined as a window with the range of 21 time points, filter numbers for three convolutional layers are 64, 32, 16 separately. The stride of convolutional layer is 1 and zero padding is also applied to make sure the size of the input unchanged. The stride of max pooling is set as 2 and window size with length of 2, which makes the input size becomes half of its original length after going through each max pooling layer. Relu activation function is used to avoid vanishing gradient problem which also makes the training process much faster [104]. The model is trained by rmsprop optimizer that divides the learning rate for a weight by a running average of the magnitudes of recent gradients for that weight and categorical cross entropy is used as loss function. Training batch size is set as 128 and epoch is set as 50 to ensure the convergence of the training process. As we know, we cannot pass the entire dataset into the neural network at once, so we need to divide the whole dataset into several batches. Here, batch size refers to the total number of training examples present in a single batch and epoch is defined as one pass of the full training set. Besides, all the input rs-fMRI time series are normalized before training or testing. In our design, a single gyri/sulci or 2-hinge/3-hinge joint classification model was trained for each subject, but all the training models shared a same 1D-CNN architecture. For gyri/sulci classifiers, the size of training samples for a single subject can reach 70,000-120,000 for BNI data and 100,000-160,000 for EMC data. For 2-hinge/3-hinge classifiers, the size of training sample can reach 40,000-80,000 for both BNI data and EMC data. Besides, for all classifiers, 70% of the extracted rs-fMRI signals from a single subject were used for training process, where 20% of the input samples were used for validation purpose in order to avoid overfitting. To evaluate classification performance, the remaining 30% rs-fMRI signals were used for testing.

3.5 Analysis on learned characteristic features in 1D-CNN

To better explore the intrinsic functional differences between gyri and sulci/2-hinge and 3-hinge joints, further analysis on the internal behaviors of learned 1D-CNN model is needed. The reason for the good classification performance of CNN model is that it can directly extract class specific characteristic features. Here, we define feature as the pattern of the weights obtained from the CNN filters. In general, the most characteristic features can be learned from the last convolutional layer in the model, the nearest one to the final classifier (Dense layer). Therefore, we put our focus on analyzing the filters of the last convolutional layer (CONV3) and the weights of each filter are learned during training process. As mentioned in Section 3.4, in our proposed 1D-CNN model, each filter in the last convolutional layer is corresponding to two weights in softmax layer. It can be seen from Figure 3.3, GA layers have the same number of nodes (neurons) with the number of filters in CONV3 and Dense layer has two nodes. Here, for each node in GA layer, it has a relationship to the corresponding filter in CONV3. Thus, weight value of each connection between nodes in GA layer and the node in Dense layer can decide the filter type (gyral/sulcal filter or 2-hinge/3hinge filter) to a certain degree. Before training, each input rs-fMRI time series comes with a label, either 0 for sulci and 1 for gyri or 0 for 2-hinge and 1 for 3-hinge. After the input goes through all the layers in the model, it can derive a final output from the two nodes in Dense layer, the value of which for both nodes is between 0 and 1 since a softmax function is used. If the output value is larger than 0.5 for a sulci/2-hinge node, the input signal will be assigned a label 0 and if the output value is larger than 0.5 for a gyri/3-hinge node, the input signal will be assigned a label 1. According to our predefined labels (sulci:0, gyri:1 or 2-hinge:0, 3-

hinge:1), if the weight value of each connection between nodes in GA layer and the nodes in Dense layer is positive for sulci node but negative for gyri node, then its corresponding filter is much likely to be a sulci or 2-hinge filter; otherwise, it is much likely to be a gyri or 3-hinge filter. The reason that we can determine a filter type in such a way is because the outputs of Relu activation function are all non-negative which can result in all non-negative outputs for GA layer as well. Therefore, the positive weight value is more likely to contribute to a larger probability output for a certain type of node, however, the negative weight value works in an opposite way. Based on the sign of a weight value for the connection between the GA nodes and a certain type of node in Dense layer, the corresponding filter type will be confirmed. After the decision of a certain filter type is made, we apply an analysis on these features derived from filters of the last convolutional layer in the frequency domain. The frequency domain of features can be derived by applying fast Fourier transform (FFT) on the original filters and their visualizations and interpretations are provided in Section 4.

4. Results

Based on the methods described above, this section mainly presents two subsequent findings. The first finding is related to the classification results of gyri/sulci or 2-hinge/3-hinge joint rs-fMRI signals in both healthy and patient groups at individual level. In terms of the classification accuracy based on testing data, it can reach more than 90% for gyri/sulci rs-fMRI signal differentiation, more than 80% for 2-hinge/3-hinge joint rs-fMRI signal differentiation for every single subject, either control or patient. The other finding is derived from the frequency domain analysis on the learned high-level features defined as the pattern of weights from filters in the last convolutional layer. From the visualization of filters (features) in frequency domain, we can observe a quite different frequency distribution pattern between gyral and sulcal filters or between 2-hinge and 3-hinge filters which once again confirms the different functional roles of neural activities under resting state in gyri and sulci, as well as 2-hinge and 3-hinge gyral folding joints on the basis of the good classification performance. Interestingly, such differences can be found in both healthy controls and autism patients and the frequency distribution pattern of certain type of filters in both groups are quite similar which indicated that similar differences in functional roles of either gyri/sulci or 2-hinge/3-hinge exist in all experimental subjects, no matter they are healthy or diseased.

4.1 Classification Accuracy of gyri/sulci and 2-hinge/3-hinge joint rs-fMRI signals

The classification accuracy with a corresponding standard deviation based on the testing result for each group is summarized in Table 3.1, where each value is the averaged one across the corresponding group. It can be seen that the overall differentiability between 2-hinge and 3-hinge joint rs-fMRI signals is not as good as that between sulci and gyri rs-fMRI signals. However, the classification result is still good enough, much better than chance level, which indicates possible intrinsically different functional roles of gyri/sulci and 2-hinge/3-hinge joints. For the 10% average accuracy gap between gyral/sulcal and 2-hinge/3-hinge joint rs-fMRI signal classification, it may ascribe to two reasons: 1. Since 2-hinge/3-hinge gyral joints all belong to gyral folding regions, the rs-fMRI signals extracted from different hinge regions but all from gyral region may not that differentiable from each other compared with the rs-fMRI signal classification of gyri/sulci. 2. The 6mm radius in separating 2-hinge and 3-hinge gyral regions may result in some false positive and false negative anatomical labels although it is quite reasonable from visualization. However, more than 80% percent classification accuracy is still 30% more than chance level and it can be seen from the feature filters extracted from 2-hinge/3-hinge classification models that 2-hinge and 3-hinge rs-fMRI signals do have their corresponding characteristic features in frequency domain. Besides, we can also observe that there are rare differences between healthy controls and autism patients from a single institution in terms of classification accuracy for classifying either gyri/sulci or 2-hinge/3hinge joint rs-fMRI signals. Meanwhile, the classification accuracy remains quite stable although across different institutions and such a reproducible result indicates the good performance of our proposed model architecture in differentiating gyri/sulci or 2-hinge/3hinge joint rs-fMRI signals.

Table 3.2. Average testing classification accuracy

BNI				EMC			
gyri/sulci		2-hinge/3-hinge		gyri/sulci		2-hinge/3-hinge	
control	patient	control	patient	control	patient	control	patient
mean accuracy		mean accuracy		mean accuracy		mean accuracy	
94.48%	95.15%	87.03%	87.58%	94.00%	95.35%	88.07%	87.88%
standard deviation		standard deviation		standard deviation		standard deviation	
0.0217	0.0228	0.0348	0.0345	0.0177	0.0237	0.0316	0.0342

4.2 Gyral/sulcal and 2-hinge/3-hinge filters in frequency domain

In the experiment, filters can be derived from all models trained from all subjects, which means the actual number of all filters we can obtain is much larger than the ones we presented in Figure 3.4(a). However, according to our observation, many of the filters learned from different subjects are quite similar. Therefore, we did a clustering analysis on all of the learned filters of a certain type (gyral, sulcal, 2-hinge, 3hinge) in the frequency domain from the same group (control/patient) for both of the two institutions (BNI and EMC). What we can see here are the ones derived by averaging all the filters in the same cluster.

From Figure 3.4(a), we can observe that for both control and patient groups, there are two main frequency distribution patterns in sulcal filters, one is that the medium frequency band tend to keep relatively high magnitude, such as the patterns in blue and green from sulci-control and patterns in blue from sulci-patient in Figure 3.5(a); the other is that a U shape pattern occurs in the medium frequency band which corresponds to a lower magnitude. However, the second pattern still has some sub-patterns where the width of the medium frequency band for the U shape and its corresponding magnitude are somewhat different. Besides, the bilateral frequency bands right near the U shape tend to keep relatively high magnitude. In gyral filters, it presents a quite different situation where the magnitude in all frequency band is much lower (mostly less than 0.5) compared with those in sulcal filters. In 3-hinge filters, most frequency band exhibits a relatively low magnitude and a flat tendency compared with those in 2-hinge filters. Interestingly, we can find that the characteristic frequency domain 3-hinge filter type is a subtype of the derived gyral filters in frequency domain. This finding is quite consistent with the fact that three hinges are extracted from gyral regions. For the 2-hinge specific characteristic features, the magnitude in all frequency bands tend to be relatively low as well. From Figure 3.4(b), we can also find out a similar frequency distribution pattern of all types of filters learned from different groups based on the data of EMC institution.

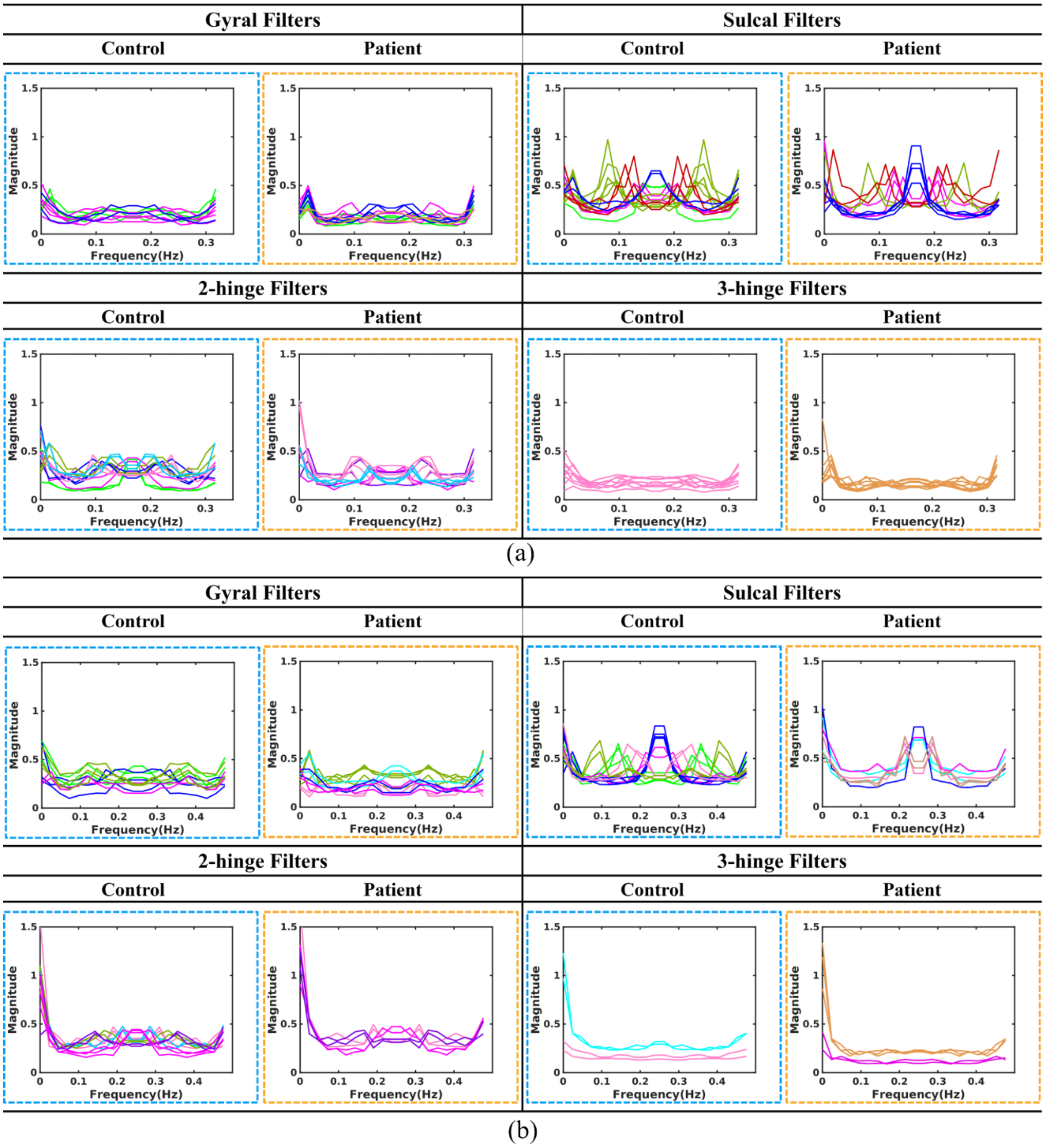

Figure 3.4. Filter features learned from 1D-CNN model based on data from two institutions. (a) BNI; (b) EMC. The frequency distributions for gyral, sulcal, 2-hinge and 3-hinge filters of both control and patient group. Frequency distribution of filters in similar shape are represented by the same color and different colors are used for different shape types.

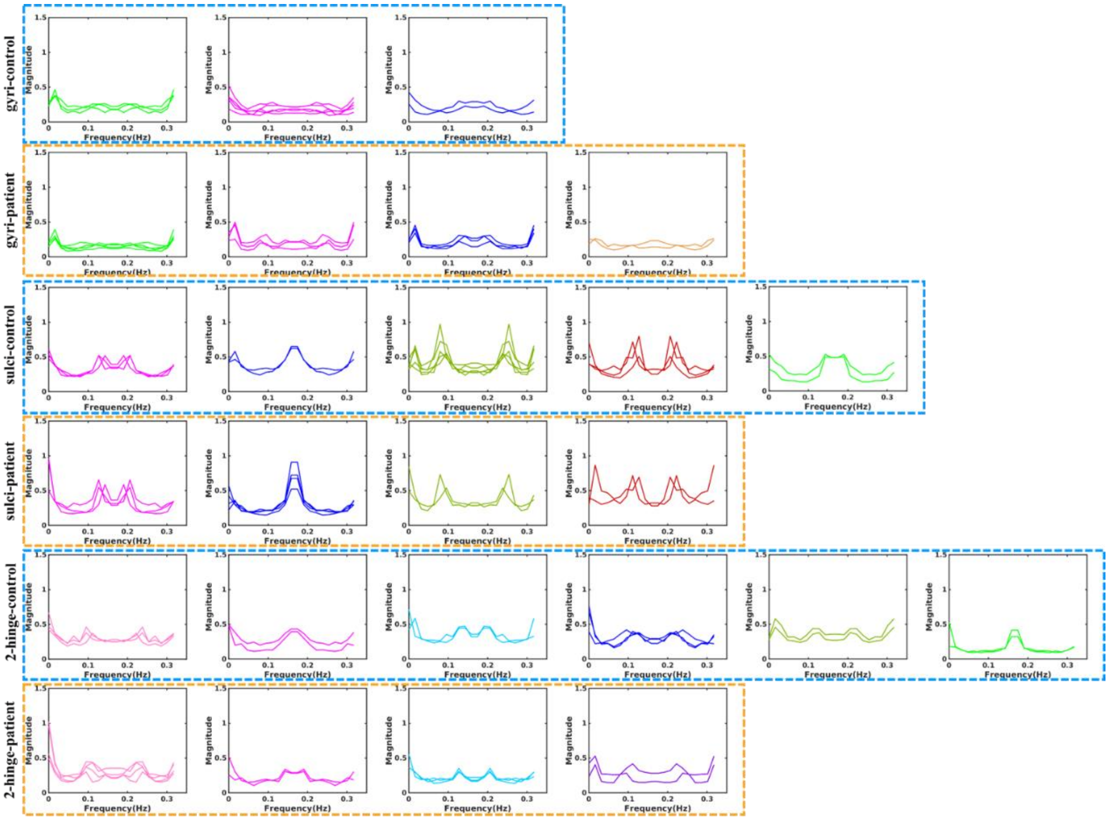
gyri-control
gyri-patient
sulci-control
sulci-patient
2-hinge-control
2-hinge-patient
Magnitude
Frequency(Hz)
0
0.5
1
1.5
0.1
0.2
0.3

(a)

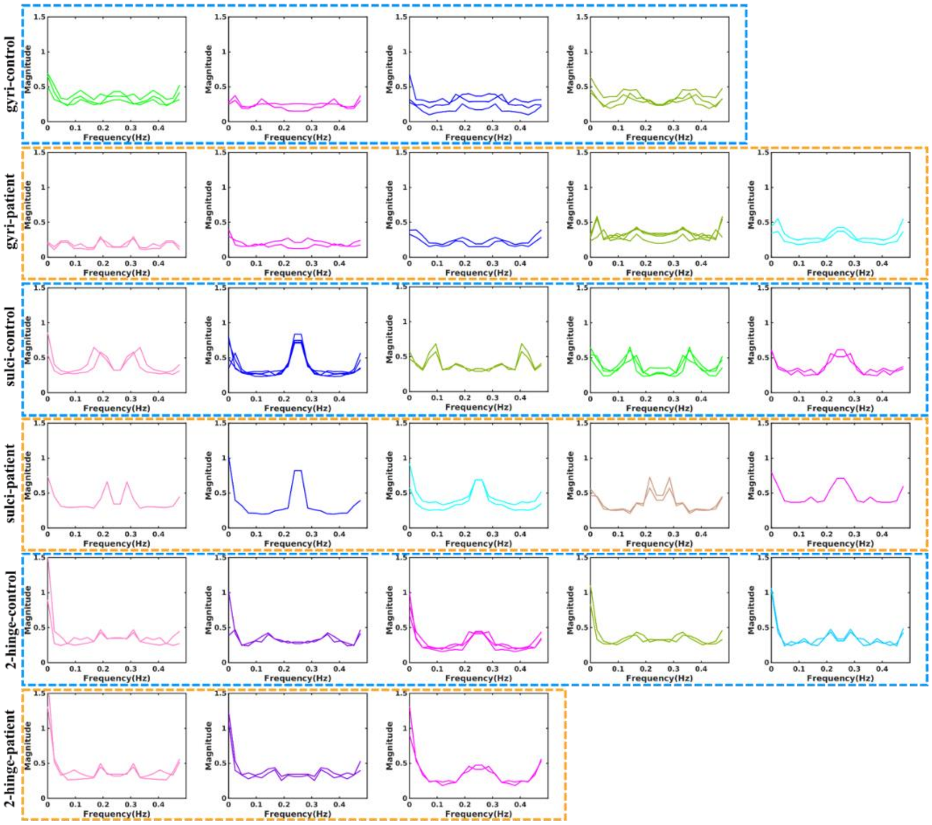
gyri-control
gyri-patient
sulci-control
sulci-patient
2-hinge-control
2-hinge-patient
Magnitude
Frequency(Hz)
0
0.5
1
1.5
0.1
0.2
0.3
0.4

(b)

Figure 3.5. Separate visualization of filter (gyral, sulcal, 2-hinge) frequency distributions in different shapes for each group. (a) BNI; (b) EMC. The parts circled by the dashed box with the same color (blue/orange) are results belonging to the same group (control/patient).

In addition, we can observe that the frequency distribution patterns of certain type of filter are quite similar for most of the cases in both groups. Considering the individual variabilities across institutes, even within a single institute, our result so far is robust enough to unveil the different functional roles exhibited by rs-fMRI signals of gyri/sulci and 2-hinge/3-hinge in both control and patient groups. Meanwhile, we also put some selected original filters in time domain here as can be seen in Figure 3.6.

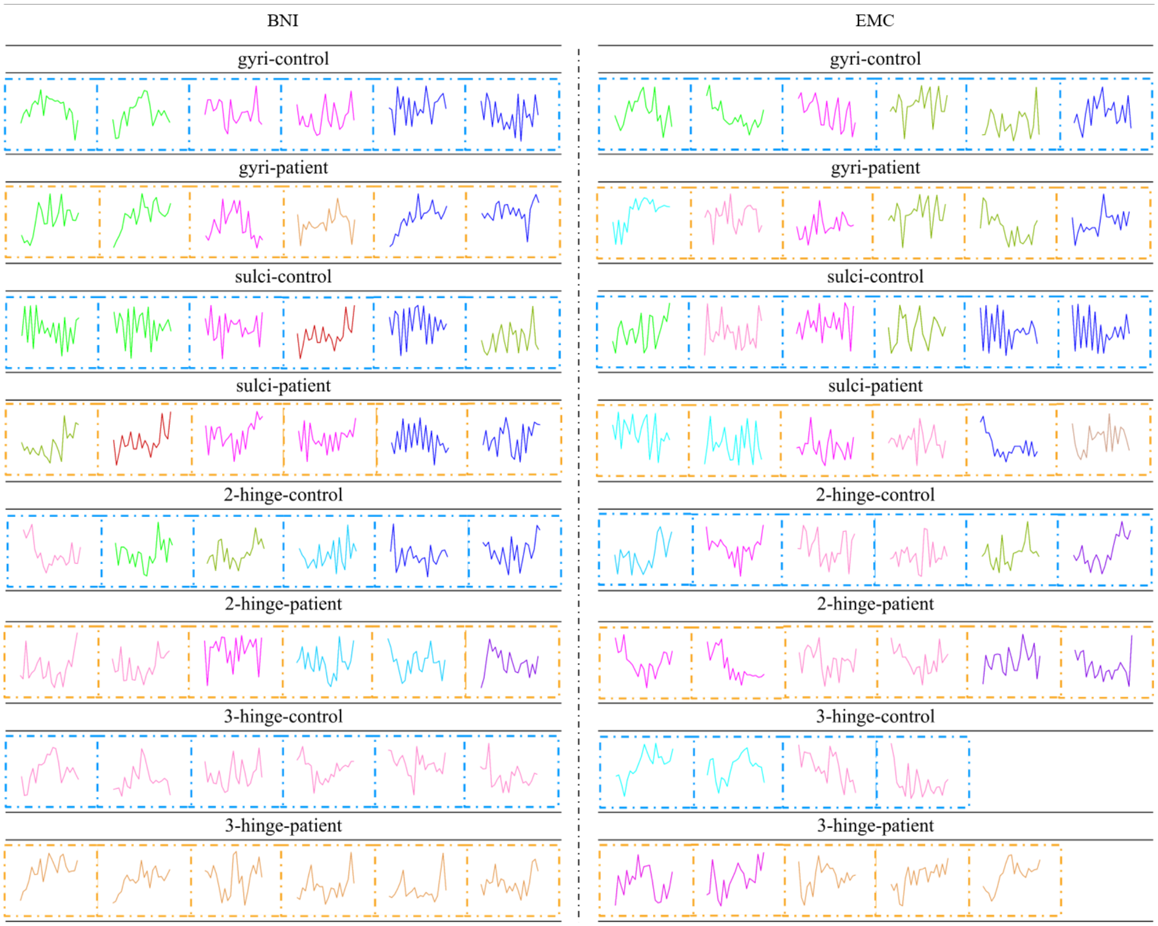

Figure 3.6. Selected original filters of gyri, sulci, 2-hinge and 3-hinge in both control and patient group from two institutions. Six representative original filters are selected for each type (gyri, sulci, 2-hinge or 3-hinge) in each group (control or patient). Here, the color of different filters has a correspondence to that in Figure 3.4 and Figure 3.5.

5. Discussion and Conclusion

In this work, classification models based on 1D-CNN method are designed and applied in differentiating gyral and sulcal or 2-hinge and 3-hinge joint rs-fMRI signals. An average classification accuracy of 94.24% for controls, 95.24% for patients or 87.53% for controls, 87.72% for patients has been achieved. Further analysis on the internal behaviors of the learned models was also performed and differences of filter features in frequency domain were observed. Since certain frequency distribution can be used to represent certain pattern of functional features, the observed results in Section 4 are meaningful to unveil functional roles of gyri/sulci and 2-hinge/3-hinge rs-fMRI joint signals. Specifically, 3-hinges on gyri with lower rhythms might play major roles in reflecting long distance communication and performing global functional integration, while sulci with higher rhythms tend to be in charge of local information processing and are critical for segregation of brain areas. Using rs-fMRI data for autism study as a test bed, we can also conclude that the observed differences not only exist in healthy population, but also in autism disease group.

In terms of the frequency distribution of the filters of certain type (gyri, sulci, 2-hinge or 3-hinge), we have not observed an obvious difference existing between healthy controls and autism patients so far. Following this line of study, further work can be extended and enhanced in more specific brain anatomical areas such as superior frontal gyrus and central sulcus for deeper investigations of possible mechanisms of functional segregations of gyri and sulci or 2-hinge and 3-hinge. Moreover, exploration of the differences between control and patient group can also concentrate on some specific predefined anatomical areas and analyze separately instead of focusing on the whole cortical surface together. Another interesting extension to the present work would be applying more powerful representation learning models with optimized architecture by using neural architecture search (NAS).

CHAPTER 4

OPTIMIZING CNN MODEL FOR FMRI SIGNAL CLASSIFICATION VIA ADANET-BASED NEURAL ARCHITECTURE SEARCH[3]

---

[3] Haixing Dai*, Fangfei Ge*, Qing Li, Wei Zhang and Tianming Liu. “Optimize CNN Model for fMRI Signal Classification via AdaNet-based Neural Architecture Search.” Submitted to International Conference on Medical Image Computing and Computer-Assisted Intervention (MICCAI), 2019.

1. Abstract

The content in this chapter is a follow up work of Chapter 3. The work in previous chapter has explored the different functional roles among gyral, sulcal and 2-hinge and 3-hinge rsfMRI signals via 1D-CNN models from functional perspective. Here, I extend my previous work in terms of model architecture by optimizing the framework of CNN models using a neural architecture search (NAS) system.

Recent studies showed that convolutional neural network (CNN) models possess remarkable capability of differentiating and characterizing fMRI signals from cortical gyri and sulci. In addition, visualization and analysis of the filters in the learned CNN models suggest that sulcal fMRI signals are more diverse and have higher frequency than gyral signals. However, it is not clear whether the gyral fMRI signals can be further divided into sub-populations, e.g., 3-hinge areas vs 2-hinge areas. It is also unclear whether the CNN models of two classes (gyral vs sulcal) classification can be further optimized for three classes (3-hinge gyral vs 2-hinge gyral vs sulcal) classification. To answer these questions, in this chapter, we employed the AdaNet framework to design a neural architecture search (NAS) system for optimizing CNN models for three classes fMRI signal classification. The core idea is that AdaNet adaptively learns both the optimal structure of the CNN network and its weights so that the learnt CNN model can effectively extract discriminative features that maximize the classification accuracies of three classes of 3-hinge gyral, 2-hinge gyral and sulcal fMRI signals. We evaluated our framework on the Autism Brain Imaging Data Exchange (ABIDE) dataset, and experiment results show that our framework can obtained significantly better results, in terms of both classification accuracy and extracted features.

2. Background and Motivation

The human cerebral cortex is characterized by highly convoluted regions which fold themselves into gyri and sulci [3, 4, 43, 45, 83]. Many previous literature studies have reported the fundamental structural and functional differences between gyri and sulci by analyzing multimodal neuroimaging data. For instance, a recent study used convolutional neural networks (CNN) to differentiate and characterize fMRI signals extracted from gyri and sulci [38, 39], and it turned out that sulcal fMRI signals are more diverse and have higher frequency than gyral signals. Detailed analysis and visualization of the filters in the learnt CNN models suggest that the cerebral cortex might be bisectionally segregated into two fundamentally different functional units of gyri and sulci [38, 39]. In those studies, the powerful CNN model played a major role in extracting meaningful filter features that contributed to the differentiation of gyral and sulcal fMRI signals, demonstrating the great promise of using deep learning methods for fMRI data analysis and neuroscience discovery research.

Though the studies in [38, 39] significantly advanced our fundamental understanding of the intrinsic difference between gyri and sulci, there are several key unanswered questions. First, it is not clear whether the gyral fMRI signals can be further divided into sub-populations, e.g., 3-hinge areas (where 3 different gyral crests meet) [86] vs 2-hinge areas, as illustrated in the blue and red areas in Figure 4.1, the detailed parcellation criteria of which can refer to Section 3.3 in Chapter 3. It has been reported that those 3-hinge gyral areas have significantly higher fiber densities than 2-hinge areas (measured by diffusion tensor imaging (DTI) data) [86], and thus it is reasonable to hypothesize that those 3-hinge gyral regions might play different functional roles from 2-

hinge gyral areas. Hence, it will be of interest to examine the three classes fMRI signal classification problem, that is, 3-hinge gyral vs 2-hinge gyral vs sulcal signal classification. In addition, it is unclear whether the CNN models of two classes (gyral vs sulcal) classification used in prior studies [38, 39] can be further optimized for three classes (3-hinge gyral vs 2-hinge gyral vs sulcal) classification, e.g., in terms of the neural network structures and hyper-parameters. Since existing deep learning networks such as CNNs have been manually designed and their structures and hyperparameters could be substantially optimized and improved via the recent neural architecture search (NAS) framework [105, 106]. It is reasonable to hypothesize that the optimized CNN networks could better represent and extract more meaningful features from real fMRI dataset.

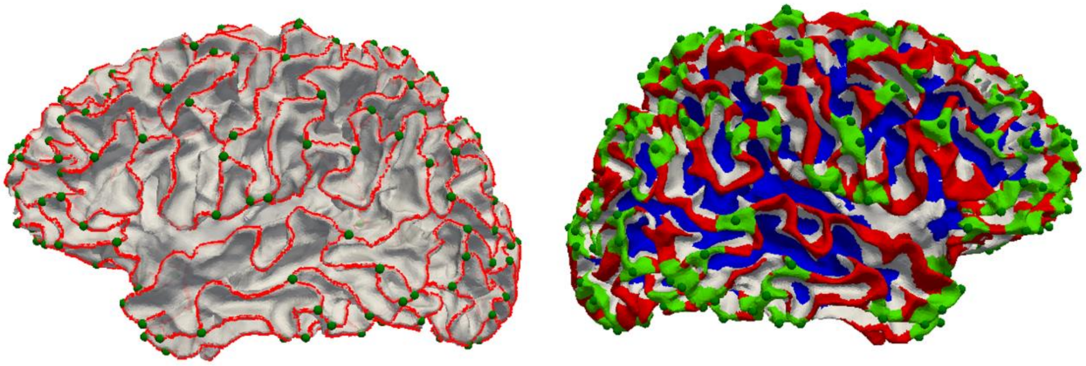

Figure 4.1. Illustration of the three classes classification problem. (a) Illustration of gyral net across the cortical surface (red curves) and 3-hinge gyri center (dark green sphere). (b) Parcellation of the cortex into three classes of 3-hinge gyri (green), 2-hinge gyri (red) and sulci (blue). The left and right figures are mirrored and both from left hemisphere.

To address the abovementioned questions and test above hypotheses, in this chapter, we designed a novel neural architecture search (NAS) system to optimize CNN models for three classes fMRI signal classification based on the AdaNet framework

[105]. The key idea is that the AdaNet framework can adaptively learn both the optimal structure of the CNN network and its weights so that the learnt CNN model can effectively extract discriminative features that maximize the classification accuracies among three classes of 3-hinge gyral, 2-hinge gyral and sulcal fMRI signals. Based on these optimized CNN model and extracted features, we are then able to test the abovementioned hypotheses about three classes classification and CNN network optimization. To that end, we evaluated our framework on the public available Autism Brain Imaging Data Exchange (ABIDE) dataset, and extensive experiments showed that our framework can obtained significantly better results, in terms of both classification accuracy and extracted meaningful features.

3. Methods

3.1 Data description and preprocessing

Experimental data used in this study were downloaded from the publicly available Autism Brain Imaging Data Exchange (ABIDE) II. The ABIDE was established for discovery science on the brain connectome in autism spectrum disorder (ASD). Here, we used the dataset from BNI (Barrow Neurological Institute) as our test bed. According to manually checked preprocessing results, 58 subjects (29 control and 29 patients) from BNI are considered as high quality and thus selected. Please refer to http://fcon_1000.projects.nitrc.org/indi/abide/abide_II.html for detailed information. Then we randomly selected 20 samples of these 58 subjects for our experiment. Preprocessing for the resting state fMRI (rsfMRI) data were performed using the FSL software tools, including skull removal, motion correction, spatial smoothing, temporal pre-whitening, slice time correction, global drift removal, and linear registration to the Montreal Neurological Institute (MNI) standard brain template space, which were all implemented by using FSL and other tools based on FreeSurfer.

3.2 Neural architecture search (NAS) and AdaNet

A key step in designing a multi-layer deep neural network for a specific task is the selection of the network's architecture, e.g., the number of layers and the number of neurons in each layer. Though the CNN model for two classes classification in [38, 39] has achieved promising results, its number of layers and the number of neurons in each layer are decided by manual experience and thus they might not be optimal in various senses. Recently, a powerful framework of neural architecture search (NAS) has been proposed in the literature [106], and several NAS systems have shown promising results in traditional image classification problems [105-107].

In this chapter, we adopt the recently published AdaNet framework [105] as our NAS engine. In the AdaNet framework, instead of enforcing a pre-defined neural network architecture with a fixed network complexity, the system adaptively searches and learns the appropriate network architecture for a specific task. Briefly, the AdaNet starts with a simple linear model (illustrated in Figure 4.2), and then the system gradually augments the network with more neurons and additional layers, as much as needed. This incremental search process is the core of the neural network search and optimization process. Naturally, the addition of subnetworks (as shown in Figure 4.2) depends on their complexity and is directly constrained by the learning criteria. Importantly, it has been shown that the AdaNet's optimization process is strongly convex and thus it is guaranteed to converge to a unique global solution [105]. Thus, based on the AdaNet

NAS engine, our framework will optimize CNN model with the objective of maximizing classification accuracy among three classes, as illustrated in Figure 4.2. The NAS framework is specifically explained in the figure and its legend.

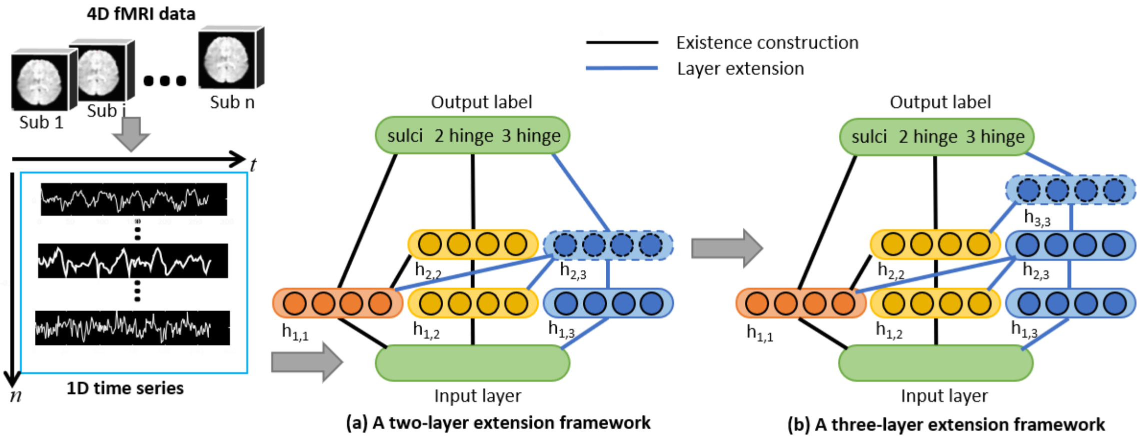

(a) A two-layer extension framework

(b) A three-layer extension framework

Figure 4.2. Illustration of our NAS framework based on AdaNet. The time series of fMRI data is considered as the input of our model. Then we optimize the neural network structures with the objective of maximizing the classification accuracy among three classes of sulci, 2-hinge gyri, and 3-hinge gyri fMRI signals. The gray arrow illustrates the neural structure search step. Additional implementation details are provided in Section 3.3.

More specifically, in this framework, we used the momentum as the optimizer of the AdaNet based NAS. Momentum is the gradient decent with a short-memory as follows:

$$\mathrm{z}^{k+1} = \beta z^{k} + \nabla f(w^{k}) \tag{4.1}$$

$$\mathrm{w}^{k+1} = w^{k} - \alpha \mathrm{z}^{k+1} \tag{4.2}$$

In this equation, when the learning rate (β) equals 0, we recover the gradient decent. But for $\beta = 0.99$, this appears to be the boost we need. So, our iterations regain that speed and boldness it lost, speeding to the optimum with a renewed energy. Based on the procedures above, the NAS framework is implemented based on the Auto-ML system [8], which is summarized as follows (Table 4.1):

Table 4.1. Algorithm for NAS

Algorithm1. Neural Architecture Search (NAS)

```
Input: S is the initial network, N as the iteration number.
Output: $S_{best}$
$S_{best} \longleftarrow 0$
for $(i = 0$ to $N)$
    $S_1, S_2 \longleftarrow$ GetNewNetwork$(S)$
    $w_1, w_2 \longleftarrow$ EvaluaeNetwork$(S_1, S_2)$
    if $w_2$ is better than $w_1$ then
        $S_{best\_i} \longleftarrow S_2, w_{best\_i} \longleftarrow w_2$
    else  $S_{best\_i} \longleftarrow S_1, w_{best\_i} \longleftarrow w_1$
    $S^* \longleftarrow$ GetNewNetwork$(S)$
    $w^* \longleftarrow$ EvaluaeNetwork$(S^*)$
    if $w^*$ is better than $w_{best\_i}$ then
        $S_{best\_i} \longleftarrow S^*, w_{best\_i} \longleftarrow w^*$
    else  return $S_{best\_i}$
end
return$(S_{best\_N})$
```

To be more specific, we have two options to generate a new network: for the first option, we can generate the new network by adding a connection between the units in layer i and the units in layer $i - 1$; the second option is generating a new network by adding a deeper layer. The option selection is based on the best reduction of the current value of the optimal function. These options are also illustrated in Figure 4.2.

3.3 Implementation details

In this work, the designed 1D CNN framework based on NAS took one dimensional rsfMRI time series data as input, which were normalized before training or testing. Here, each time series of length 115 was extracted according to its corresponding anatomical parcellated location as explained in Figure 4.1, after which it will be assigned a label as sulci, 2-hinge gyri or 3-hinge gyri. After fMRI signal extraction and labeling, the size of training samples for a single ABIDE subject is around 80,000-120,000. For all classifiers, 70% of the extracted fMRI signals were used for training, while the remaining 30% fMRI signals were used for testing. Specifically, 20 subjects (10 healthy controls and 10 patients) from ABIDE II dataset were randomly used as our test bed and a corresponding model was trained for each individual subject. In our NAS framework based on Adanet, the base network was initialized with a simple CNN with only one convolutional layer and one max-pooling layer followed by one global average pooling layer and a dense layer for classification output. For hyperparameters, the filter length was set as 64, the kernel size as 32, the learning rate as 0.05, the maximum training step as 8000, and the batch size as 5400. Besides, the Adanet iteration was set as 3. After three iterations, we can obtain the optimized CNN model based on the initialized CNN.

4. Results

4.1 Classification results

To evaluate the robustness of our proposed method, we not only implemented a 3-class classification, but also implemented a 2-class classification experiment based on sulcal and gyral fMRI signals. Figure 4.3 and Figure 4.4 show the classification results of 2-class and 3-class classifications based on testing data. We can observe that, for 2-class classification, the testing accuracy can be improved by 4~5% by using NAS framework compared with the results from CNN model without NAS optimization. Meanwhile, for 3-class classification, the testing accuracy can be improved by approximately 10%, which is a truly significant improvement achieved by NAS.

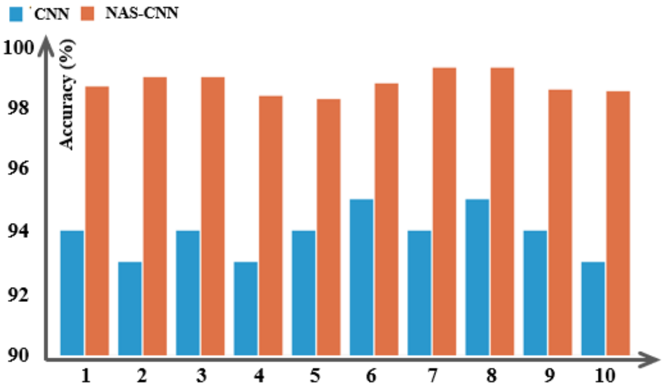

Figure 4.3. Testing accuracy for 10 randomly selected subjects in 2-class classification. The orange bars represent the accuracy of models via NAS framework and the blue bars represent the accuracy of CNN model without NAS optimization.

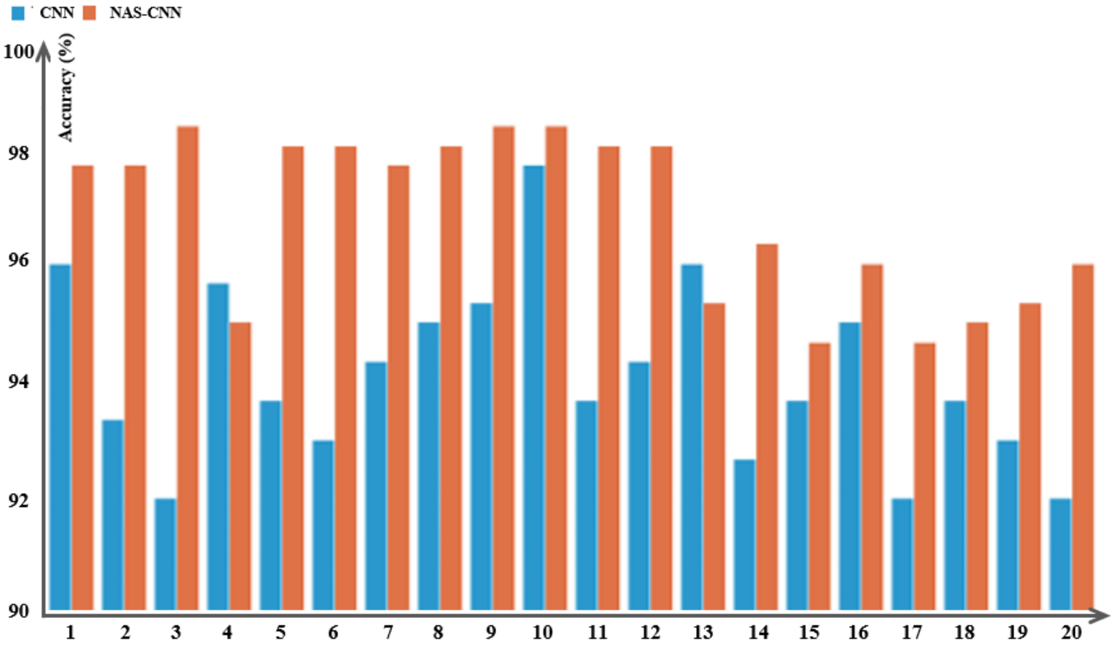

Figure 4.4. Testing accuracy for 20 randomly selected subjects in 3-class classification. The orange bars represent the accuracy of models via NAS framework and the blue bars represent the accuracy of CNN model without NAS optimization.

To further examine the testing accuracy differences in CNN models with and without NAS optimization, we displayed the confusion matrices in 3-class classifications, as shown in Fig. 5. From both matrices, we can observe that sulcal fMRI signals can be differentiated much better than 2-hinge and 3-hinge signals since the anatomical location of 2-hinge and 3-hinge regions on cortical surface all belong to gyri. In CNN model without optimization, about half of the 3-hinge signals were classified as 2-hinge. However, the differentiation accuracy between 2-hinge and 3-hinge fMRI signals can be largely improved by CNN model optimized by the NAS framework, demonstrating the effectiveness of our framework based on NAS in improving the classification power of CNN models. This result also suggests that 2-hinge gyri and 3-hinge gyri might have quite different functional roles, as we hypothesized in the introduction section.

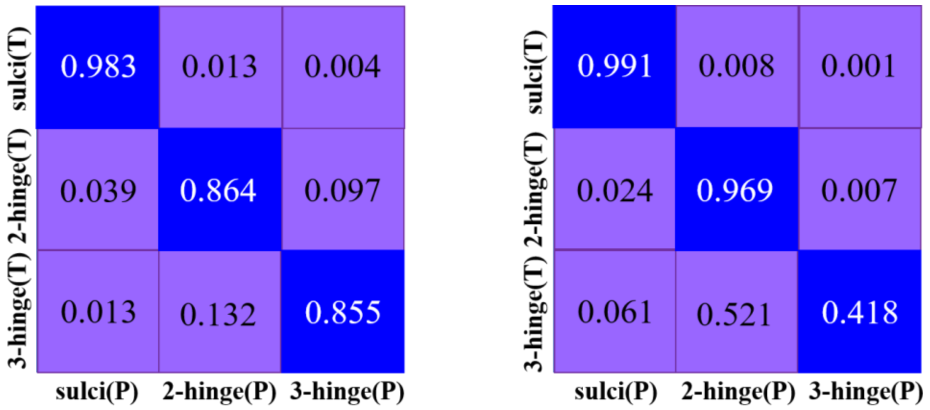

	sulci(P)	2-hinge(P)	3-hinge(P)
sulci(T)	0.983	0.013	0.004
2-hinge(T)	0.039	0.864	0.097
3-hinge(T)	0.013	0.132	0.855

(a)

	sulci(P)	2-hinge(P)	3-hinge(P)
sulci(T)	0.991	0.008	0.001
2-hinge(T)	0.024	0.969	0.007
3-hinge(T)	0.061	0.521	0.418

(b)

Figure 4.5. The confusion matrix for average testing accuracy. The left one is the result of models using NAS framework. The right one is the result of CNN without NAS optimization. T in the bracket means the ground truth of a label and P in the bracket is the prediction result.

4.2 Analysis of learnt filters in NAS-optimized CNN

In addition to the classification result in Figures 4.3-4.5, we also examined the different types of filters learnt in the CNN model to further understand their frequency characteristics. In Figure 4.6, we visualize three types of filters (sulcal, 2-hinge, 3-hinge) using their time series patterns. Specifically, we can observe that for sulcal filters, there exists several frequency distribution patterns, and most of them tend to exhibit relatively high magnitude, as shown in the left side of Figure 4.6. In gyral filters, we find that the magnitudes in all frequency bands are lower compared with those in sulcal filters, which agrees with literature report [38]. In 3-hinge filters, most frequency bands exhibit a relatively low magnitude and a flat tendency compared with those in 2-hinge filters. To better understand the extracted filters, we also mapped the GA (Global Average) layer activation back to the corresponding cortical surfaces, as shown in Figure 4.7. Interestingly, from the mapping results of sulcal filters, most of the sulcal regions presented a higher activation, while for those corresponding to 2-hinge and 3-hinge filters, 2-hinge and 3-hinge regions tended to have a higher activation accordingly which also can be seen from Figure 4.7.

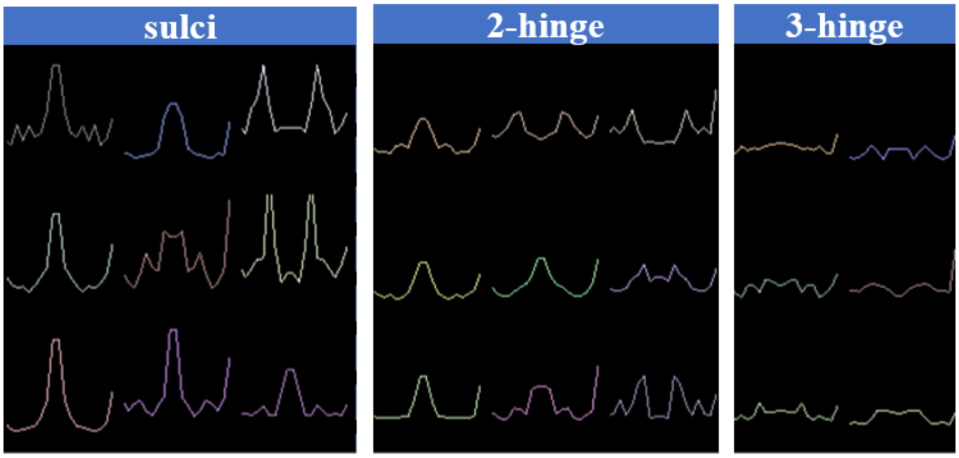

Figure 4.6. Visualization of filter signals of sulci, 2-hinge gyri and 3-hinge gyri.

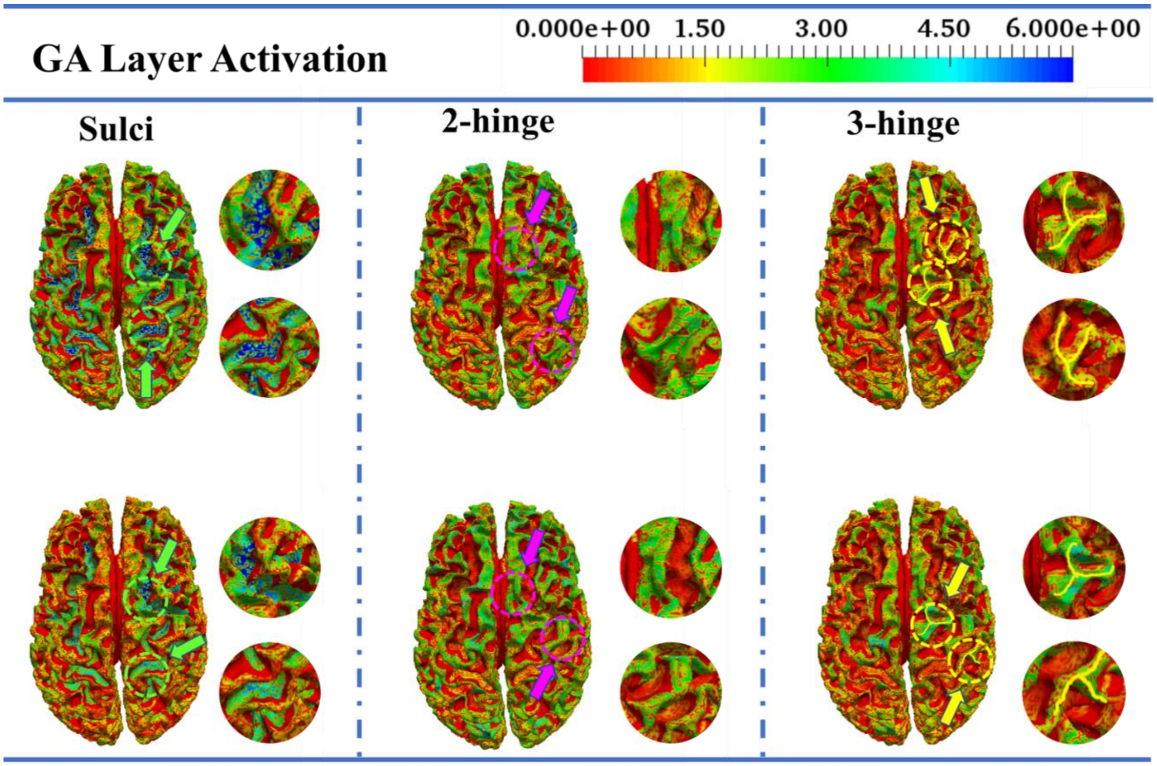

Figure 4.7. Global Average (GA) layer activation corresponding to sulcal, 2-hinge and 3-hinge filters. Here, we randomly selected two mapping results for each type of signal filter to present. For each type of signal filter, two representative regions with higher activations (blue or green colors) are circled and zoomed-in for better visualization.

5. <u>Discussion and Conclusion</u>

In this chapter, we presented a novel neural architecture search framework to optimize CNN models for three classes fMRI signal classification by using AdaNet as NAS engine. Our major methodological contribution is that AdaNet-based NAS framework can adaptively learn both the optimal structure of the CNN network and its weights so that the learnt CNN model can effectively extract discriminative features with the objective of maximizing the classification accuracies among three classes of 3-hinge gyral, 2-hinge gyral and sulcal fMRI signals. We evaluated the NAS-optimized CNNs on the public available ABIDE II dataset, and experimental results showed that our framework can obtain significantly better classification accuracy. Also, visualization and interpretation of the extracted filters by NAS-optimized CNNs suggested neuro-scientifically meaningful results. Overall, our work demonstrated the promise of using NAS for optimizing deep learning models of fMRI data and offered novel insights into the structure-function relationships between cortical folding (e.g., 2-hinge gyri and 3-hinge gyri) and brain function.

CHAPTER 5

CONCLUSION AND FUTURE WORK

This dissertation summarizes the major research work during my doctoral study. To conclude, the dissertation contributes to the analysis of cortical 3-hinge gyral joint from both structural and functional perspective. For 3-hinge structural analysis (Chapter 2), the experiment results consistently show that DTI-derived fiber densities in 3-hinge regions are much higher than those in 2-hinge regions, suggesting that during gyrification gyral regions with higher concentrations of growing axonal fibers tend to form 3-hinge gyri. The proposed integrative approach combining neuroimaging data analysis and computational modeling appears effective in probing a plausible theory of 3-hinge gyri formation and providing new insights into structural and functional cortical architectures and their relationship. For 3-hinge functional analysis (Chapter 3-4), it investigates and confirms different functional roles of neural activities under resting state in gyri and sulci, as well as 2-hinge and 3-hinge gyral folding joints in both healthy subjects and autism groups. Specifically, Chapter 4 presents a novel neural architecture search (NAS) framework to optimize CNN models in Chapter 3 by using AdaNet as NAS engine. Corresponding experiment results showed the NAS framework can obtain significantly better results, in terms of both classification accuracy and extracted features.

The future work of this research topic can be further investigated in the following directions. First, from the structural perspective, the typical 3-hinge brain anatomical pattern can potentially serve as landmarks to improve cortical registration performance since conventional image registration methods based on anatomical morphology could hardly align such diverse cortical patterns at a fine-grained resolution. Therefore, some related work can be proposed following this line of research to further explore the unique and useful role of 3-hinge in cortical registration. Second, for the functional study of 3-hinge gyral joints in Chapter 3, further work can be extended and enhanced in more specific brain anatomical areas such as superior frontal gyrus and central sulcus for deeper investigations of possible mechanisms of functional segregations of gyri and sulci or 2-hinge and 3-hinge. Moreover, exploration of the differences between control and patient group can also concentrate on some specific predefined anatomical areas and analyze separately instead of focusing on the whole cortical surface together.

REFERENCES

[1] E. Armstrong, A. Schleicher, H. Omran, M. Curtis, and K. Zilles, "The ontogeny of human gyrification," *Cerebral cortex,* vol. 5, no. 1, pp. 56-63, 1995.

[2] T. White, S. Su, M. Schmidt, C.-Y. Kao, and G. Sapiro, "The development of gyrification in childhood and adolescence," *Brain and cognition,* vol. 72, no. 1, pp. 36-45, 2010.

[3] P. Rakic, "Specification of cerebral cortical areas," *Science,* vol. 241, no. 4862, pp. 170-176, 1988.

[4] K. Zilles *et al.*, "Quantitative analysis of sulci in the human cerebral cortex: development, regional heterogeneity, gender difference, asymmetry, intersubject variability and cortical architecture," *Human brain mapping,* vol. 5, no. 4, pp. 218-221, 1997.

[5] B. Fischl, M. I. Sereno, and A. M. Dale, "Cortical surface-based analysis: II: inflation, flattening, and a surface-based coordinate system," *Neuroimage,* vol. 9, no. 2, pp. 195-207, 1999.

[6] D. C. Van Essen, "A tension-based theory of morphogenesis and compact wiring in the central nervous system," *NATURE-LONDON-,* pp. 313-318, 1997.

[7] T. Liu, D. Shen, and C. Davatzikos, "Deformable registration of cortical structures via hybrid volumetric and surface warping," *NeuroImage,* vol. 22, no. 4, pp. 1790-1801, 2004.

[8] K. Li *et al.*, "Gyral folding pattern analysis via surface profiling," *NeuroImage,* vol. 52, no. 4, pp. 1202-1214, 2010.

[9] B. Fischl *et al.*, "Cortical folding patterns and predicting cytoarchitecture," *Cerebral cortex,* vol. 18, no. 8, pp. 1973-1980, 2007.

[10] J. N. Giedd *et al.*, "Brain development during childhood and adolescence: a longitudinal MRI study," *Nature neuroscience,* vol. 2, no. 10, p. 861, 1999.

[11] M. Schaer, M. B. Cuadra, L. Tamarit, F. Lazeyras, S. Eliez, and J.-P. Thiran, "A surface-based approach to quantify local cortical gyrification," *IEEE transactions on medical imaging,* vol. 27, no. 2, pp. 161-170, 2008.

[12] B. Fischl and A. M. Dale, "Measuring the thickness of the human cerebral cortex from magnetic resonance images," *Proceedings of the National Academy of Sciences,* vol. 97, no. 20, pp. 11050-11055, 2000.

[13] I. H. Smart, C. Dehay, P. Giroud, M. Berland, and H. Kennedy, "Unique morphological features of the proliferative zones and postmitotic compartments of the neural epithelium giving rise to striate and extrastriate cortex in the monkey," *Cerebral cortex,* vol. 12, no. 1, pp. 37-53, 2002.

[14] V. A. Magnotta *et al.*, "Quantitative in vivo measurement of gyrification in the human brain: changes associated with aging," *Cerebral Cortex,* vol. 9, no. 2, pp. 151-160, 1999.

[15] F. Deng *et al.*, "A functional model of cortical gyri and sulci," *Brain structure and function,* vol. 219, no. 4, pp. 1473-1491, 2014.

[16] J. Nie, L. Guo, G. Li, C. Faraco, L. S. Miller, and T. Liu, "A computational model of cerebral cortex folding," *Journal of theoretical biology,* vol. 264, no. 2, pp. 467-478, 2010.

[17] C. C. Hilgetag and H. Barbas, "Developmental mechanics of the primate cerebral cortex," *Anatomy and embryology*, vol. 210, no. 5-6, p. 411, 2005.

[18] X. Jiang *et al.*, "Sparse representation of HCP grayordinate data reveals novel functional architecture of cerebral cortex," *Human brain mapping,* vol. 36, no. 12, pp. 5301-5319, 2015.

[19] X. Jiang *et al.,* "Temporal dynamics assessment of spatial overlap pattern of functional brain networks reveals novel functional architecture of cerebral cortex," *IEEE Transactions on Biomedical Engineering*, 2016.

[20] X. Jiang *et al.*, "Modeling functional dynamics of cortical gyri and sulci," in *International Conference on Medical Image Computing and Computer-Assisted Intervention*, 2016, pp. 19-27: Springer.

[21] G. Li, W. Lin, J. H. Gilmore, and D. Shen, "Spatial patterns, longitudinal development, and hemispheric asymmetries of cortical thickness in infants from birth to 2 years of age," *Journal of Neuroscience,* vol. 35, no. 24, pp. 9150-9162, 2015.

[22] M. D. Budde and J. Annese, "Quantification of anisotropy and fiber orientation in human brain histological sections," *Frontiers in integrative neuroscience*, vol. 7, p. 3, 2013.

[23] E. Takahashi, R. D. Folkerth, A. M. Galaburda, and P. E. Grant, "Emerging cerebral connectivity in the human fetal brain: an MR tractography study," *Cerebral cortex,* vol. 22, no. 2, pp. 455-464, 2011.

[24] H. Chen *et al.*, "Coevolution of gyral folding and structural connection patterns in primate brains," *Cerebral Cortex,* p. bhs113, 2012.

[25] T. Zhang *et al.*, "Characterization of U-shape streamline fibers: Methods and applications," *Medical image analysis,* vol. 18, no. 5, pp. 795-807, 2014.

[26] J. Nie *et al.*, "Axonal fiber terminations concentrate on gyri," *Cerebral cortex,* vol. 22, no. 12, pp. 2831-2839, 2011.

[27] G. Li, T. Liu, D. Ni, W. Lin, J. H. Gilmore, and D. Shen, "Spatiotemporal patterns of cortical fiber density in developing infants, and their relationship with cortical thickness," *Human brain mapping,* vol. 36, no. 12, pp. 5183-5195, 2015.

[28] X. Li *et al.*, "Commonly preserved and species-specific gyral folding patterns across primate brains," *Brain Structure and Function,* vol. 222, no. 5, pp. 2127-2141, 2017.

[29] X. Yu, H. Chen, T. Zhang, X. Hu, L. Guo, and T. Liu, "Joint analysis of gyral folding and fiber shape patterns," in *Biomedical Imaging (ISBI), 2013 IEEE 10th International Symposium on*, 2013, pp. 85-88: IEEE.

[30] H. Liu *et al.*, "Elucidating functional differences between cortical gyri and sulci via sparse representation HCP grayordinate fMRI data," *Brain research,* vol. 1672, pp. 81-90, 2017.

[31] H. Chen *et al.*, "Evolutionarily-preserved consistent gyral folding patterns across primate brains," in *Biomedical Imaging (ISBI), 2014 IEEE 11th International Symposium on*, 2014, pp. 1218-1221: IEEE.

[32] H. Chen, Y. Li, F. Ge, G. Li, D. Shen, and T. Liu, "Gyral net: A new representation of cortical folding organization," *Medical image analysis,* vol. 42, pp. 14-25, 2017.

[33] C.-H. Chen *et al.*, "Hierarchical genetic organization of human cortical surface area," *Science,* vol. 335, no. 6076, pp. 1634-1636, 2012.

[34] K. Zilles, E. Armstrong, A. Schleicher, and H.-J. Kretschmann, "The human pattern of gyrification in the cerebral cortex," *Anatomy and embryology,* vol. 179, no. 2, pp. 173-179, 1988.

[35] B. T. Yeo, P. Yu, P. E. Grant, B. Fischl, and P. Golland, "Shape analysis with overcomplete spherical wavelets," in *International Conference on Medical Image Computing and Computer-Assisted Intervention*, 2008, pp. 468-476: Springer.

[36] G. Li *et al.*, "Mapping longitudinal development of local cortical gyrification in infants from birth to 2 years of age," *Journal of Neuroscience,* vol. 34, no. 12, pp. 4228-4238, 2014.

[37] R. Toro *et al.*, "Brain size and folding of the human cerebral cortex," *Cerebral cortex,* vol. 18, no. 10, pp. 2352-2357, 2008.

[38] H. Liu *et al.*, "The Cerebral Cortex is Bisectionally Segregated into Two Fundamentally Different Functional Units of Gyri and Sulci," *Cerebral Cortex,* 2018.

[39] S. Zhang *et al.*, "Deep Learning Models Unveiled Functional Difference between Cortical Gyri and Sulci," *IEEE Transactions on Biomedical Engineering*, 2018.

[40] X. Li *et al.*, "Commonly preserved and species-specific gyral folding patterns across primate brains," *Brain Structure and Function,* pp. 1-15, 2016.

[41] T. Sun and R. F. Hevner, "Growth and folding of the mammalian cerebral cortex: from molecules to malformations," *Nature Reviews Neuroscience,* vol. 15, no. 4, pp. 217-232, 2014.

[42] S. Budday, P. Steinmann, and E. Kuhl, "Secondary instabilities modulate cortical complexity in the mammalian brain," *Philosophical Magazine,* vol. 95, no. 28-30, pp. 3244-3256, 2015.

[43] G. Lohmann, D. Y. Von Cramon, and A. C. Colchester, "Deep sulcal landmarks provide an organizing framework for human cortical folding," *Cerebral Cortex,* vol. 18, no. 6, pp. 1415-1420, 2008.

[44] F. H. Gilles, A. Leviton, and E. Dooling, *The developing human brain: growth and epidemiologic neuropathology*. Butterworth-Heinemann, 2013.

[45] D. P. Richman, R. M. Stewart, J. W. Hutchinson, and V. S. Caviness Jr, "Convolutional Development," 1975.

[46] T. Tallinen, J. Y. Chung, F. Rousseau, N. Girard, J. Lefèvre, and L. Mahadevan, "On the growth and form of cortical convolutions," *Nature Physics*, 2016.

[47] J. Dubois *et al.*, "Primary cortical folding in the human newborn: an early marker of later functional development," *Brain,* vol. 131, no. 8, pp. 2028-2041, 2008.

[48] J. N. Giedd and J. L. Rapoport, "Structural MRI of pediatric brain development: what have we learned and where are we going?," *Neuron,* vol. 67, no. 5, pp. 728-734, 2010.

[49] G. Li *et al.*, "Mapping longitudinal development of local cortical gyrification in infants from birth to 2 years of age," *The Journal of Neuroscience,* vol. 34, no. 12, pp. 4228-4238, 2014.

[50] K. Zilles *et al.*, "Quantitative analysis of sulci in the human cerebral cortex: development, regional heterogeneity, gender difference, asymmetry, intersubject variability and cortical architecture," *Human brain mapping,* vol. 5, no. 4, pp. 218-221, 1997.

[51] B. Fischl *et al.*, "Cortical folding patterns and predicting cytoarchitecture," *Cerebral cortex,* vol. 18, no. 8, pp. 1973-1980, 2008.

[52] P. M. Thompson *et al.*, "Mapping cortical change in Alzheimer's disease, brain development, and schizophrenia," *Neuroimage,* vol. 23, pp. S2-S18, 2004.

[53] C. W. Nordahl *et al.*, "Cortical folding abnormalities in autism revealed by surface-based morphometry," *The Journal of Neuroscience,* vol. 27, no. 43, pp. 11725-11735, 2007.

[54] E. Bullmore and O. Sporns, "Complex brain networks: graph theoretical analysis of structural and functional systems," *Nature Reviews Neuroscience,* vol. 10, no. 3, pp. 186-198, 2009.

[55] C. J. Honey, J.-P. Thivierge, and O. Sporns, "Can structure predict function in the human brain?," *Neuroimage,* vol. 52, no. 3, pp. 766-776, 2010.

[56] R. Toro and Y. Burnod, "A morphogenetic model for the development of cortical convolutions," *Cerebral cortex*, vol. 15, no. 12, pp. 1900-1913, 2005.

[57] J. Nie *et al.*, "Axonal fiber terminations concentrate on gyri," *Cerebral Cortex*, vol. 22, no. 12, pp. 2831-2839, 2012.

[58] P. Bayly, L. Taber, and C. Kroenke, "Mechanical forces in cerebral cortical folding: a review of measurements and models," *Journal of the mechanical behavior of biomedical materials*, vol. 29, pp. 568-581, 2014.

[59] P. T. Schoenemann, "Evolution of the size and functional areas of the human brain," *Annu. Rev. Anthropol.*, vol. 35, pp. 379-406, 2006.

[60] C. Honey *et al.*, "Predicting human resting-state functional connectivity from structural connectivity," *Proceedings of the National Academy of Sciences*, vol. 106, no. 6, pp. 2035-2040, 2009.

[61] T. Liu, "A few thoughts on brain ROIs," *Brain imaging and behavior*, vol. 5, no. 3, pp. 189-202, 2011.

[62] J. Neal, M. Takahashi, M. Silva, G. Tiao, C. A. Walsh, and V. L. Sheen, "Insights into the gyrification of developing ferret brain by magnetic resonance imaging," *Journal of anatomy*, vol. 210, no. 1, pp. 66-77, 2007.

[63] A. Cachia *et al.*, "A mean curvature based primal sketch to study the cortical folding process from antenatal to adult brain," in *International Conference on Medical Image Computing and Computer-Assisted Intervention*, 2001, pp. 897-904: Springer.

[64] A. Cachia *et al.*, "A primal sketch of the cortex mean curvature: a morphogenesis based approach to study the variability of the folding patterns," *IEEE transactions on medical imaging*, vol. 22, no. 6, pp. 754-765, 2003.

[65] A. Y. Hardan, R. J. Jou, M. S. Keshavan, R. Varma, and N. J. Minshew, "Increased frontal cortical folding in autism: a preliminary MRI study," *Psychiatry Research: Neuroimaging*, vol. 131, no. 3, pp. 263-268, 2004.

[66] P. Yu, B. T. T. Yeo, P. E. Grant, B. Fischl, and P. Golland, "Cortical folding development study based on over-complete spherical wavelets," in *2007 IEEE 11th International Conference on Computer Vision*, 2007, pp. 1-8: IEEE.

[67] L. Ronan *et al.*, "Differential tangential expansion as a mechanism for cortical gyrification," *Cerebral Cortex*, vol. 24, no. 8, pp. 2219-2228, 2014.

[68] D. C. Van Essen *et al.*, "The Human Connectome Project: a data acquisition perspective," *Neuroimage*, vol. 62, no. 4, pp. 2222-2231, 2012.

[69] T. Liu, J. Nie, A. Tarokh, L. Guo, and S. T. Wong, "Reconstruction of central cortical surface from brain MRI images: method and application," *NeuroImage*, vol. 40, no. 3, pp. 991-1002, 2008.

[70] M. Jenkinson, C. F. Beckmann, T. E. Behrens, M. W. Woolrich, and S. M. Smith, "Fsl," *Neuroimage*, vol. 62, no. 2, pp. 782-790, 2012.

[71] B. Fischl, "FreeSurfer," *Neuroimage*, vol. 62, no. 2, pp. 774-781, 2012.

[72] T. Zhang, M. J. Razavi, X. Li, H. Chen, T. Liu, and X. Wang, "Mechanism of Consistent Gyrus Formation: an Experimental and Computational Study," *Scientific Reports*, vol. 6, 2016.

[73] T. Tallinen, J. Y. Chung, J. S. Biggins, and L. Mahadevan, "Gyrification from constrained cortical expansion," *Proceedings of the National Academy of Sciences,* vol. 111, no. 35, pp. 12667-12672, 2014.

[74] P. Bayly, R. Okamoto, G. Xu, Y. Shi, and L. Taber, "A cortical folding model incorporating stress-dependent growth explains gyral wavelengths and stress patterns in the developing brain," *Physical biology,* vol. 10, no. 1, p. 016005, 2013.

[75] M. J. Razavi, T. Zhang, T. Liu, and X. Wang, "Cortical folding pattern and its consistency induced by biological growth," *Scientific reports,* vol. 5, 2015.

[76] T. Zhang *et al.*, "Mechanisms of circumferential gyral convolution in primate brains," *Journal of computational neuroscience,* vol. 42, no. 3, pp. 217-229, 2017.

[77] Y. Cao, Y. Jiang, B. Li, and X. Feng, "Biomechanical modeling of surface wrinkling of soft tissues with growth-dependent mechanical properties," *Acta Mechanica Solida Sinica,* vol. 25, no. 5, pp. 483-492, 2012.

[78] M. J. Razavi and X. Wang, "Morphological patterns of a growing biological tube in a confined environment with contacting boundary," *RSC Advances,* vol. 5, no. 10, pp. 7440-7449, 2015.

[79] M. J. Razavi, R. Pidaparti, and X. Wang, "Surface and interfacial creases in a bilayer tubular soft tissue," *Physical Review E,* vol. 94, no. 2, p. 022405, 2016.

[80] S. Budday *et al.*, "Mechanical properties of gray and white matter brain tissue by indentation," *Journal of the mechanical behavior of biomedical materials,* vol. 46, pp. 318-330, 2015.

[81] M. J. Razavi, T. Zhang, X. Li, T. Liu, and X. Wang, "Role of mechanical factors in cortical folding development," *Physical Review E*, vol. 92, no. 3, p. 032701, 2015.

[82] M. A. Holland, K. E. Miller, and E. Kuhl, "Emerging brain morphologies from axonal elongation," *Annals of biomedical engineering*, vol. 43, no. 7, pp. 1640-1653, 2015.

[83] E. R. Kandel *et al.*, *Principles of neural science*. McGraw-hill New York, 2000.

[84] J. Dubois *et al.*, "Primary cortical folding in the human newborn: an early marker of later functional development," *Brain*, vol. 131, no. 8, pp. 2028-2041, 2008.

[85] G. H. Davis and S. J. Reynolds, "Structural geology of rocks and regions," in *Structural geology of rocks and regions. 2nd edition*: Wiley, 1996.

[86] F. Ge *et al.*, "Denser Growing Fiber Connections Induce 3-hinge Gyral Folding," *Cerebral Cortex*, pp. 1-12, 2017.

[87] A. Krizhevsky, I. Sutskever, and G. E. Hinton, "Imagenet classification with deep convolutional neural networks," in *Advances in neural information processing systems*, 2012, pp. 1097-1105.

[88] R. Girshick, J. Donahue, T. Darrell, and J. Malik, "Region-based convolutional networks for accurate object detection and segmentation," *IEEE transactions on pattern analysis and machine intelligence*, vol. 38, no. 1, pp. 142-158, 2016.

[89] T. Wang, D. J. Wu, A. Coates, and A. Y. Ng, "End-to-end text recognition with convolutional neural networks," in *Pattern Recognition (ICPR), 2012 21st International Conference on*, 2012, pp. 3304-3308: IEEE.

[90] D. Cireşan, U. Meier, and J. Schmidhuber, "Multi-column deep neural networks for image classification," *arXiv preprint arXiv:1202.2745*, 2012.

[91] S. Lai, L. Xu, K. Liu, and J. Zhao, "Recurrent Convolutional Neural Networks for Text Classification," in *AAAI*, 2015, vol. 333, pp. 2267-2273.

[92] Y. LeCun, Y. Bengio, and G. Hinton, "Deep learning," *nature,* vol. 521, no. 7553, p. 436, 2015.

[93] E. Hosseini-Asl, G. Gimel'farb, and A. El-Baz, "Alzheimer's Disease Diagnostics by a Deeply Supervised Adaptable 3D Convolutional Network," *arXiv preprint arXiv:1607.00556,* 2016.

[94] M. Ghafoorian *et al.*, "Deep multi-scale location-aware 3D convolutional neural networks for automated detection of lacunes of presumed vascular origin," *NeuroImage: Clinical,* vol. 14, pp. 391-399, 2017.

[95] Y. Zhao *et al.,* "Automatic Recognition of fMRI-derived Functional Networks using 3D Convolutional Neural Networks," *IEEE Transactions on Biomedical Engineering,* 2017.

[96] H. Huang *et al.*, "Modeling task fMRI data via deep convolutional autoencoder," *IEEE transactions on medical imaging,* vol. 37, no. 7, 2018.

[97] Y. Zhao, F. Ge, and T. Liu, "Automatic recognition of holistic functional brain networks using iteratively optimized convolutional neural networks (IO-CNN) with weak label initialization," *Medical image analysis,* vol. 47, pp. 111-126, 2018.

[98] T. Stephan *et al.*, "Functional MRI of galvanic vestibular stimulation with alternating currents at different frequencies," *Neuroimage,* vol. 26, no. 3, pp. 721-732, 2005.

[99] J. F. Kleine, W. O. Guldin, and A. H. Clarke, "Variable otolith contribution to the galvanically induced vestibulo-ocular reflex," *Neuroreport,* vol. 10, no. 5, pp. 1143-1148, 1999.

[100] W. H. Thompson and P. Fransson, "The frequency dimension of fMRI dynamic connectivity: network connectivity, functional hubs and integration in the resting brain," *NeuroImage,* vol. 121, pp. 227-242, 2015.

[101] X.-N. Zuo *et al.*, "The oscillating brain: complex and reliable," *Neuroimage,* vol. 49, no. 2, pp. 1432-1445, 2010.

[102] S. R. Gohel and B. B. Biswal, "Functional integration between brain regions at rest occurs in multiple-frequency bands," *Brain connectivity,* vol. 5, no. 1, pp. 23-34, 2015.

[103] M. Lin, Q. Chen, and S. Yan, "Network in network," *arXiv preprint arXiv:1312.4400,* 2013.

[104] A. F. Agarap, "Deep Learning using Rectified Linear Units (ReLU)," *arXiv preprint arXiv:1803.08375,* 2018.

[105] C. Cortes, X. Gonzalvo, V. Kuznetsov, M. Mohri, and S. Yang, "Adanet: Adaptive structural learning of artificial neural networks," in *Proceedings of the 34th International Conference on Machine Learning-Volume 70,* 2017, pp. 874-883: JMLR. org.

[106] B. Zoph and Q. V. Le, "Neural architecture search with reinforcement learning," *arXiv preprint arXiv:1611.01578*, 2016.

[107] T. Elsken, J. H. Metzen, and F. Hutter, "Neural architecture search: A survey," *arXiv preprint arXiv:1808.05377*, 2018.